Draft version December 4, 2025
Typeset using LaTeX **twocolumn** style in AASTeX631



# A Comprehensive JWST/NIRSpec Census of Broad-Line Active Galactic Nuclei: Faint, Tiny, but Highly Accreting Sources in the Remote Universe

Caroline J. Baccus [1,2] and Xinfeng Xu [3,4]

[1] *Menlo School, Atherton, CA, USA*
[2] *New York University, 726 Broadway Rm. 1005, New York, NY 10003, USA*
[3] *Center for Interdisciplinary Exploration & Research in Astrophysics (CIERA), Evanston, IL, USA*
[4] *Department of Physics and Astronomy, Northwestern University, 2145 Sheridan Road, Evanston, IL, 60208, USA*

(Revised December 4, 2025)

## ABSTRACT

We present a sample of 252 broad-line Active Galactic Nuclei (BLAGNs), incorporating 171 newly identified sources, spanning a redshift interval from $z = 0.8$ to 7.2. We have analyzed spectroscopic data from the NIRSpec instrument aboard the James Webb Space Telescope, using the G140H, G140M, G235H, G235M, G395H, and G395M gratings to survey N $\sim$ 80,000 galaxies for BLAGNs. Through emission-line fitting, using a sum of Gaussian models for H$\alpha$, H$\beta$, [N II] $\lambda\lambda$6548, 6584, and [O III] $\lambda\lambda$4959, 5007, we separate AGN broad-line components from narrow-line emission. We find the detection rate of BLAGNs to be relatively consistent across our redshift range. Compared to typical low-$z$ AGNs ($z \lesssim 1$), the high-$z$ BLAGNs are systematically fainter and less massive, yet they accrete more efficiently, with most showing Eddington ratios between 0.1 and 1.0. This confirms the rapid black hole growth during the early cosmic epochs. The detection of faint, low-mass BLAGNs at high redshift also helps bridge the observational gap between local supermassive black holes and remote luminous quasars, providing a more complete view of black hole-galaxy coevolution across cosmic time.

*Keywords:* galaxies: active — galaxies: distances and redshifts — galaxies: high-redshift — galaxies: nuclei — (galaxies:) quasars: emission lines —(galaxies:) quasars: supermassive black holes

## 1. INTRODUCTION

Active galactic nuclei (AGN) powered by supermassive black holes (SMBHs) are among the most luminous and energetic phenomena in the cosmos. They drive galaxy growth and shape evolutionary pathways through intense radiation, jets and outflows (e.g., Silk & Rees 1998; Hardcastle & Croston 2020; Laha et al. 2021). Observations and theoretical studies show that SMBHs coevolve with their host galaxies, with black-hole accretion and stellar-mass assembly regulating each other (e.g., Kormendy & Ho 2013; McConnell & Ma 2013). Shaped by the interplay of dark matter halos, gravitational forces, and feedback from supernovae and active galactic nuclei (AGNs), their coevolution represents a fundamental process governing galaxy evolution across cosmic time. (e.g., Hopkins et al. 2006; Fabian 2012; Mountrichas 2023).

Despite extensive observational efforts to study AGNs across a wide range of redshifts (e.g., Grogin et al. 2011; Pâris et al. 2018; Chaussidon et al. 2023), analyses of high-redshift AGNs($z \gtrsim 4$) before the launch of James Webb Space Telescope (JWST) are limited by various observational challenges. At high redshift, key AGN diagnostic lines such as [O III] $\lambda\lambda$ 4959, 5007 and H$\alpha$ are redshifted into the near-infrared (NIR), where ground-based spectroscopy suffers strong atmospheric absorption and telluric emission (e.g., Rousselot et al. 2000; Davies 2007). In addition, faintness of high-redshift AGNs in the NIR limits observations to the most luminous sources (Shen et al. 2019; Matsuoka et al. 2019; Onoue et al. 2019). This luminosity-driven selection biases samples toward high-accretion-rate SMBHs and may not represent the full AGN population at high-redshift (e.g., Mortlock et al. 2011; Banados et al. 2018).

Space-based observatories, such as the Hubble Space Telescope (HST), made the first significant breakthroughs by avoiding atmospheric interference and probing the Universe within the first few hundred million

years after the Big Bang (e.g., Beckwith et al. 2006). For example, HST's ultra-deep surveys first uncovered GN-z11 at $z \sim 11$, establishing the pre-JWST record for the most distant galaxy known (Ellis et al. 2013; Oesch et al. 2016; Bunker et al. 2023). However, with its 2.4 meter mirror and infrared cutoff $\sim 2.5$ $\mu$m, HST's sensitivity to faint, rest-frame optical emission of high-redshift AGNs remains limited, leaving the faint AGN population largely unexplored (but see, e.g., Koekemoer et al. 2011; Windhorst et al. 2011).

Though launched less than four years ago, JWST has already revolutionized our view of early-universe AGNs. Compared to previous infrared space telescope, such as Spitzer, JWST's 6.5 m primary mirror—approximately 60× Spitzer's collecting area—provides greatly enhanced infrared sensitivity. Additionally, JWST 's extended wavelength coverage up to 30 $\mu$m enables it to detect high-redshift AGNs more effectively than HST. These advancements allow JWST to reveal substantial population of lower-luminosity AGNs at $z \gtrsim 3$–4, pushing into regimes previously inaccessible (e.g., Kocevski 2022; Harikane et al. 2023; He et al. 2024; Kocevski et al. 2023; Matthee et al. 2023; Maiolino et al. 2024; Taylor et al. 2024; Juodžbalis et al. 2025). Specifically, programs including JWST Advanced Deep Extragalactic Survey (JADES) and Cosmic Evolution Early Release Science (CEERS) conduct deep NIRSpec spectroscopy that identifies faint AGNs with masses of $10^5$ – $10^8 M_\odot$, filling the gap between local SMBHs and the luminous quasars seen in previous high-redshift studies (e.g., Harikane et al. 2023; Kocevski et al. 2023; Maiolino et al. 2024; Kocevski 2022). Together, these observations highlight JWST's capability to detect larger populations of AGNs and constrain their properties at high-redshift, offering unprecedented insight into AGN evolution in the early universe.

In addition, recent findings from JWST have revealed that compared to local AGNs, high-$z$ AGNs exhibit higher bolometric luminosities and Eddington ratios as a function of black hole mass, suggesting higher accretion efficiencies and rapid black hole growth (e.g., Harikane et al. 2023; Übler et al. 2023; Lambrides et al. 2024; Suh et al. 2025). These results suggest that faint AGNs may represent an early evolutionary phase in black hole growth, and that SMBHs in the early universe grow faster than their host galaxies, enriching the universe with higher metallicity (e.g., Übler et al. 2023). However, the majority of these conclusions are based on single or small sample high-redshift AGNs (e.g., Suh et al. 2025). Therefore, their conclusions could be influenced by selection bias, as AGNs with higher accretion rates are intrinsically brighter and more easily detected, potentially leading to an overgeneralization of the accretion rates to all high-redshift AGNs.

In this work, we performed such a systematic search of broad line AGNs (BLAGNs) using the v4 reduction of the Dawn JWST Archive (DJA)[1]. We describe the observations and the DJA database in Section 2. We then present the sample selection, emission line fitting, and dust extinction correction in Section 3. After that, we present the main results in Section 4, including the catalog of identified BLAGNs and key measurable properties, including line kinematics, BH mass, luminosity, and Eddington ratio. Finally, we discuss how the properties of BLAGNs evolve over redshift in Section 5. We conclude the paper in Section 6.

We adopt a flat ΛCDM cosmology with $H_0 = 70\ \mathrm{km\,s^{-1}\,Mpc^{-1}}$ and $\Omega_M = 0.3$, according to Planck Collaboration et al. (2020).

## 2. OBSERVATIONS AND DATA

DJA is a publicly available repository of JWST, including reduced data and products, maintained by Gabriel Brammer. We adopts their most recent data release[2] (v4, Valentino et al. 2025). They reduce the raw JWST data using the standard JWST pipelines, and the details are described in Heintz et al. (2024) and de Graaff et al. (2024). In brief, raw exposures were bias-subtracted and flat-fielded, then corrected for vignetting and both local and global background. Each slit spectrum was centered, sampled onto a uniform wavelength grid, and extracted from 2D into 1D. Flux-loss corrections for extended profiles were applied via a simple source-model prescription.

From the full DJA catalogue of $\sim$ 80,000 galaxies, we selected all targets observed with NIRSpec's high- (G140H, G235H, G395H) and medium-resolution (G140M, G235M, G395M) gratings for medium- to high-redshift ($z \gtrsim 2$) targets. We then apply the redshift-reliability cuts (i.e., grade $> 2.5$ from DJA) to exclude extractions with ambiguous redshift solutions. The selected galaxies serve as the parent sample for our emission-line fitting in Section 3. These galaxies are drawn primarily the following JWST programs: AURORA (Shapley et al. 2025), BLUEJAY (Belli et al. 2024), CANUCS (Rihtaršič et al. 2025), CECILIA (Strom et al. 2023), CEERS (Finkelstein et al. 2025), EXCELS (Carnall et al. 2024), GLIMPSE (Kokorev et al. 2025), JADES (Eisenstein et al. 2023), LyC22 (Schaerer et al. 2021), RUBIES (de Graaff et al. 2025), and UNCOVER (Weaver et al. 2024).

[1] https://dawn-cph.github.io/dja/spectroscopy/nirspec/

[2] https://zenodo.org/records/15472354

## 3. ANALYSIS

### 3.1. *Selection Criteria*

To select BLAGNs, we require objects to satisfy the following criteria (see, e.g., Harikane et al. 2023).

1. The full width half maximum of the broad component ($\mathrm{FWHM_{broad}}$) of H$\alpha$ (if unavailable, H$\beta$) exceeds 1000 km s$^{-1}$.
2. The signal-to-noise ratio (SNR) of the broad component of H$\alpha$ (if unavailable, H$\beta$) exceeds 5.
3. $\mathrm{FWHM_{broad}}$ of the forbidden lines ([O III] and [N II]) needs to be below 500 km s$^{-1}$.
4. The inclusion of a broad component is statistically justified by an F-test (see Section 3.2).

The threshold of $\mathrm{FWHM_{broad}} > 1000$ km s$^{-1}$ is generally adopted to ensure high specificity to AGN-driven broad-line regions, which are not observed in purely star-forming galaxies (e.g., Harikane et al. 2023).

### 3.2. *Emission Line Fitting*

To search for broad-line AGNs signatures, we fit Gaussian profiles to strong emission lines (Harikane et al. 2023; Taylor et al. 2024). In our analysis, we simultaneously fit the H$\alpha$ + [N II]$\lambda\lambda$ 6548, 6584 complex, then the H$\beta$ + [O III] $\lambda\lambda$ 4959, 5007 complex. The local continuum is determined by a linear baseline fit to sideband intervals bracketing each complex and subtracted prior to fitting the emission lines.

We first perform a single-Gaussian fit (hereafter, model–1) to each line to serve as a baseline for the F-test. Secondly, we fit four Gaussian profiles to each line complex (hereafter, model–2). For the primary lines, i.e., H$\alpha$ and H$\beta$, we fit them with a double Gaussian profiles, including one broad and one narrow component. For other lines, i.e., [N II] and [O III], we fit them with a single Gaussian profile. For the latter, a single Gaussian is sufficient, as the high-density gas in BLAGNs suppresses the broad-component emission from these forbidden lines. Overall, the four-Gaussian-profile fitting follows the function:

$$f(\lambda) = \sum_i A_i \, \frac{1}{\sigma_i \sqrt{2\pi}} \exp\!\Big(-\frac{(\lambda - \lambda_{i0} - \lambda_i)^2}{2\,\sigma_i^2}\Big) \qquad (1)$$

where $\lambda_{i0}$ is the expected central wavelength for the primary line, $\lambda_i$ is the center shift of other lines in respect to the primary line; $A_i$ is the amplitude of each line; and $\sigma_i$ is the velocity dispersion. An example of the fitting is shown in Figure 1, where we show the data in black and error in gray. The green and blue lines represent the narrow and broad components, respectively, while the red lines are for the total flux combining the two components. In the insets, we zoom-in and highlight the region of the broad wings.

To assess the significance of the broad components, we perform an F-test using the `scipy.stats.f.ppf` function as follows:

$$F \;=\; \frac{\chi_1^2 - \chi_2^2}{p_2 - p_1} \Big/ \frac{\chi_2^2}{n - p_2} \qquad (2)$$

where $\chi_1^2$ and $\chi_2^2$ are the sum of squared residuals for model–1 and model–2, respectively. The change in degrees of freedom is given by $p_2 - p_1$. $n$ is the number of data points used in the fits. We adopt a significance level $\alpha = 0.05$ and reject the null hypothesis (that model–1 suffices) whenever the measured $F$ exceeds the critical value $F_\alpha(p_2 - p_1,\, n - p_2)$ from the F-distribution.

We fix the flux ratio for doublet lines, e.g., [N II] 6584/6548 = 2.93 and [O III] 5007/4959 = 2.98 according to atomic physics (e.g., Storey & Zeippen 2000; Osterbrock & Ferland 2006). Model parameters are optimized via maximum-likelihood fitting using the error spectrum, testing Powell, L-BFGS-B, and Nelder–Mead algorithms and adopting the solution that minimizes $\chi^2$.

We adopt a Monte Carlo approach to estimate uncertainties on all model parameters. We perform $N = 1000$ simulations, in each of which the observed fluxes are perturbed by Gaussian noise with zero mean and standard deviation equal to the $1\sigma$ flux error. Each perturbed spectrum is then refit with our emission-line model. The $1\sigma$ uncertainties on each parameter are taken as the 16th and 84th percentiles of the resulting parameter distributions.

### 3.3. *Dust Extinction Correction*

To correct the observed emission line fluxes for dust attenuation, we compute the color excess $E(B-V)$ using the Balmer decrement, defined as the ratio of the integrated flux of H$\alpha$ to H$\beta$. We adopt an intrinsic ratio of 3.1, which is more appropriate for the gas conditions in both the broad-line and narrow-line regions of AGNs (see Osterbrock & Ferland 2006; Brooks et al. 2025). The color excess is defined following Calzetti et al. (2000) as:

$$E(B-V) = 1.97 \log_{10}\left(\frac{F_{\mathrm{H}\alpha}/F_{\mathrm{H}\beta}}{3.1}\right) \qquad (3)$$

where $F_{\mathrm{H}\alpha}$ and $F_{\mathrm{H}\beta}$ are the measured fluxes of components of the H$\alpha$ and H$\beta$ emission lines (Brooks et al. 2025). Using the derived $E(B-V)$, we compute the visual extinction $A_V$ assuming an extinction ratio of $R_V = 3.1$ (Osterbrock & Ferland 2006), by

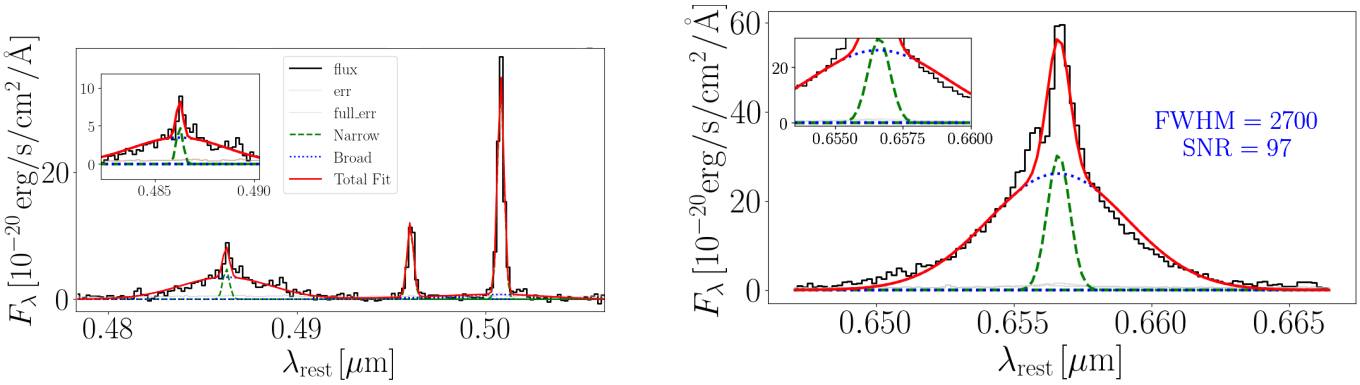


**Figure 1.** Gaussian fittings to detect BLAGN signatures for VALENTINO-3567-51909 ($z = 4.626$). We show the fittings for [O III] $\lambda\lambda$ 4959, 5007 + H$\beta$ lines (left), and H$\alpha$ + [N II]$\lambda\lambda$ 6548, 6584 (right). The NIRSpec data and errors are shown as black and gray lines, respectively. The green and blue lines are for the narrow and broad component, respectively. The red lines are the sum of both components. Inset shows an expanded view of the wing for the broad component. See Section 3.2 for the fitting details.

$$A_V = R_V \cdot E(B-V). \quad (4)$$

We then apply the Calzetti et al. (2000) attenuation curve to derive the wavelength-dependent extinction for the whole spectrum:

$$A_\lambda = k(\lambda) \cdot E(B-V), \quad (5)$$

where $k(\lambda)$ is the Calzetti attenuation law evaluated at rest-frame wavelengths. The extinction is applied to deredden the fluxes of all emission lines using the the Python package `extinction`.

## 4. RESULTS

### 4.1. *Identified BLAGNs*

Based on these selection criteria, we identify 252 BLAGNs. These objects are listed in Table 1 and their Gaussian fitting results are shown in the Appendix (Figure 7). Among the identified BLAGNs, $\sim$ 100 sources have been previously reported in the literature. Within our sample, 15 AGNs are identified from the G395H grating, 14 from G235H, 88 from G235M, 121 from the G395M grating, and 14 from the G140M grating. All identified BLAGNs exhibit prominent broad-line emission in the H$\alpha$ line or, where available, the H$\beta$ line. There are 5 sources that do not pass our criteria though previous studies identified them as BLAGNs. Our measurements yield their FWHM$_{\rm broad}$ $\sim$ 800 – 900 km s$^{-1}$, which is just below our 1000 km s$^{-1}$ criteria. To be consistent with the literature, we still keep them in the Table 1.

In Figure 2, we show the redshift distribution of our identified BLAGNs (blue histogram), where we overlay the histograms for our parent sample from DJA v4 database in red. Comparing the two distributions, we find the BLAGN detection rate is approximate uniform between $z = 2$ and 7, with the highest redshift detections at $z \sim 7.2$. The decline at $z > 7$ could be because H$\alpha$ is redshifted to the edge of NIRSpec's G395 grating, so the identification becomes more challenging.

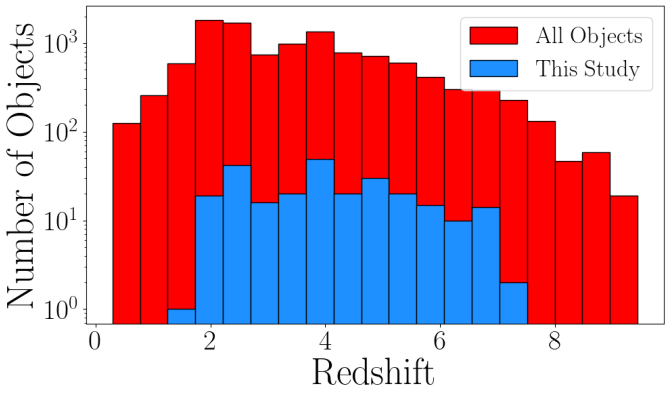


**Figure 2.** The redshift distribution of our sample of BLAGNs (blue) and the total objects searched in the DJA v4 database (red) on a log scale. The detection rates of BLAGNs is almost uniform between $z = 2$ and 7, with the highest-redshift objects out to $z = 7.2$.

### 4.2. *BH Mass Luminosity Relationship*

For each identified BLAGN, we then derive key physical parameters such as the BH mass ($M_{\rm BH}$) and bolometric luminosity (L$_{\rm bol}$) as follows.

We first computed the luminosity distance $D_L$ for each galaxy, which can be adopted to calculate the H$\alpha$ luminosity as:

$$L_{\rm H\alpha} = F_{\rm H\alpha} \times 4\pi D_L^2 \quad (6)$$

where F$_{\rm H\alpha}$ is the total broad H$\alpha$ line flux, after correcting by the $E(B-V)$ values for each object as detailed in Section 3.3. If H$\alpha$ are not covered, we adopt F$_{\rm H\alpha}$ = F$_{\rm H\beta}$ $\times$ 3.1 instead.

We then estimate $M_{\rm BH}$ using the virial method calibrated at $z \sim 0$ (Greene & Ho 2005; Matthee et al. 2023), which yields:

$$M_{\rm BH} = 2.0{\times}10^6 \left(\frac{L_{\rm H\alpha}}{10^{42}\ {\rm erg\,s^{-1}}}\right)^{0.55} \left(\frac{\rm FWHM_{H\alpha}}{10^3\ {\rm km\,s^{-1}}}\right)^{2.06} M_\odot \quad (7)$$

where $L_{\rm H\alpha}$ and $\rm FWHM_{H\alpha}$ are the luminosity and FWHM of the broad component of the H$\alpha$ emission line.

We then estimate $\rm L_{bol}$, i.e., the total energy output of the AGNs, by first scaling the $\rm L_{H\alpha}$ to the 5100 Å continuum using empirical relations, with a bolometric correction of 9.8 for standard AGNs (McLure & Dunlop 2004; Risaliti & Elvis 2004; Harikane et al. 2023; Lu et al. 2025) [3].

$$L_{\rm bol} = 9.8 \times L_{5100}. \quad (8)$$

Figure 3 shows the $\rm L_{bol}$ and BH mass our sample of AGNs (with star symbols) and ones from the literature. Our AGNs have bolometric luminosities ranging from $10^{43}\,{\rm erg^{-1}}$ to $10^{45.5}\,{\rm erg^{-1}}$, and BH masses ranging from $10^5\,M_\odot$ to $10^9\,M_\odot$. These are much lower on average then lower-redshift AGNs. The latter are shown as the contours from SDSS DR16 (Wu & Shen 2022), where the three contours represent the density distribution of AGNs enclosing 68%, 95%, and 99.7% of the total sample. This difference suggests that we cover much smaller and fainter BLAGNs in JWST. This is consistent with the findings in previous studies of high-redshift BLAGNs using deep JWST observations (e.g., Harikane et al. 2023; Maiolino et al. 2024), while our final sample size (252) is much larger than theirs (10 and 71, respectively).

In addition, there is a strong positive correlation between BH mass and $\rm L_{bol}$, which is consistent with expectations from previous studies and models of BH accretion (e.g., Harikane et al. 2023; Taylor et al. 2024; Maiolino et al. 2024). We also overlay three dashed lines representing different Eddington ratios ($\lambda_{\rm edd}$). Our identified BLAGNs commonly have $\lambda_{\rm edd}$ between 0.1 – 1.0, indicating that they are highly accreting.

### 4.3. *Velocity Width vs Broad Hα Luminosity*

In Figure 4, we show the $\rm FWHM_{H\alpha,broad}$ versus $\log(\rm L_{H\alpha,broad})$ for our sample of BLAGNs (star symbols) and others found the literature. All objects are color-code by their redshift. We find a weak positive correlation (Spearman's $\rho = 0.351$), indicating that broader H$\alpha$ lines may correspond to higher luminosities. High-$z$ BLAGNs ($z>4$) also tend to have higher $\rm L_{H\alpha,broad}$ systematically. To compare with lower redshift AGNs, we also overlay results from SDSS DR16 in contours. We find that the BLAGNs identified in our sample partially overlap with the low-redshift quasar population, suggesting that the broad-line regions (BLRs) of these high-$z$ BLAGNs may not yet be well distinguished from those of typical Type-1 quasars (see also Lin et al. 2024).

### 4.4. *Eddington Ratio Evolution with Redshift*

Harikane et al. (2023) find a tentatively trend that high-$z$ AGNs have higher Eddington ratio ($\lambda_{\rm edd}$). But their sample size is small ($\sim 10$) and suggests that more data is needed to confirm this trend. With our larger sample ($\sim 120$ AGNs with $z > 4$), we calculate $\lambda_{\rm edd}$ for each AGN similarly as theirs:

$$\lambda_{\rm Edd} = \frac{L_{\rm bol}}{L_{\rm Edd}} \quad (9)$$

where the Eddington luminosity $L_{\rm Edd}$ is defined as $L_{\rm Edd} = 1.26 \times 10^{38}\ (M_{\rm BH}/M_\odot)\ {\rm erg\,s^{-1}}$.

We find there is a clear trend that $\lambda_{\rm edd}$ decrease with increasing $M_{\rm BH}$, indicating that the more massive black holes are accreting less efficiently. This inverse relationship has been tentatively reported in previous high-redshift studies such as Harikane et al. (2023), Aggarwal (2024) and He et al. (2024). Combined with the fact that the high-redshift AGNs we identified have much lower $M_{\rm BH}$ than their low-redshift ($z<1$) counterparts (see contours in Figure 3) this indicates a strong increase in BH accretion rate in the higher-redshift universe ($z>2$).

## 5. DISCUSSION

### 5.1. *General Properties of BL AGNs over z*

Our identification of BLAGNs using JWST NIRSpec spectroscopy significantly expands the known population of AGNs at high-redshift (see Figures 2–3) and provides a larger and critical dataset for evaluating BH growth across cosmic times. Previously, similar studies commonly focused on a subset of JWST NIRSpec data (e.g., Harikane et al. 2023; Maiolino et al. 2024; Greene et al. 2024; Napolitano et al. 2025) and/or a single survey (e.g., Chien et al. 2024; Goulding et al. 2023). In contrast, our comprehensive search across the full NIRSpec database enables a more complete census of BLAGNs at high redshift.

Specifically, Harikane et al. (2023) identified a smaller sample of higher redshift AGNs which suggested that

[3] Greene et al. (2025) found that bolometric correction for Little Red Dots (LRD) is half of typical values ($\sim 5$). Since the majority of our BLAGNs do not show LRD features, we still take the value of 9.8 for standard AGNs.

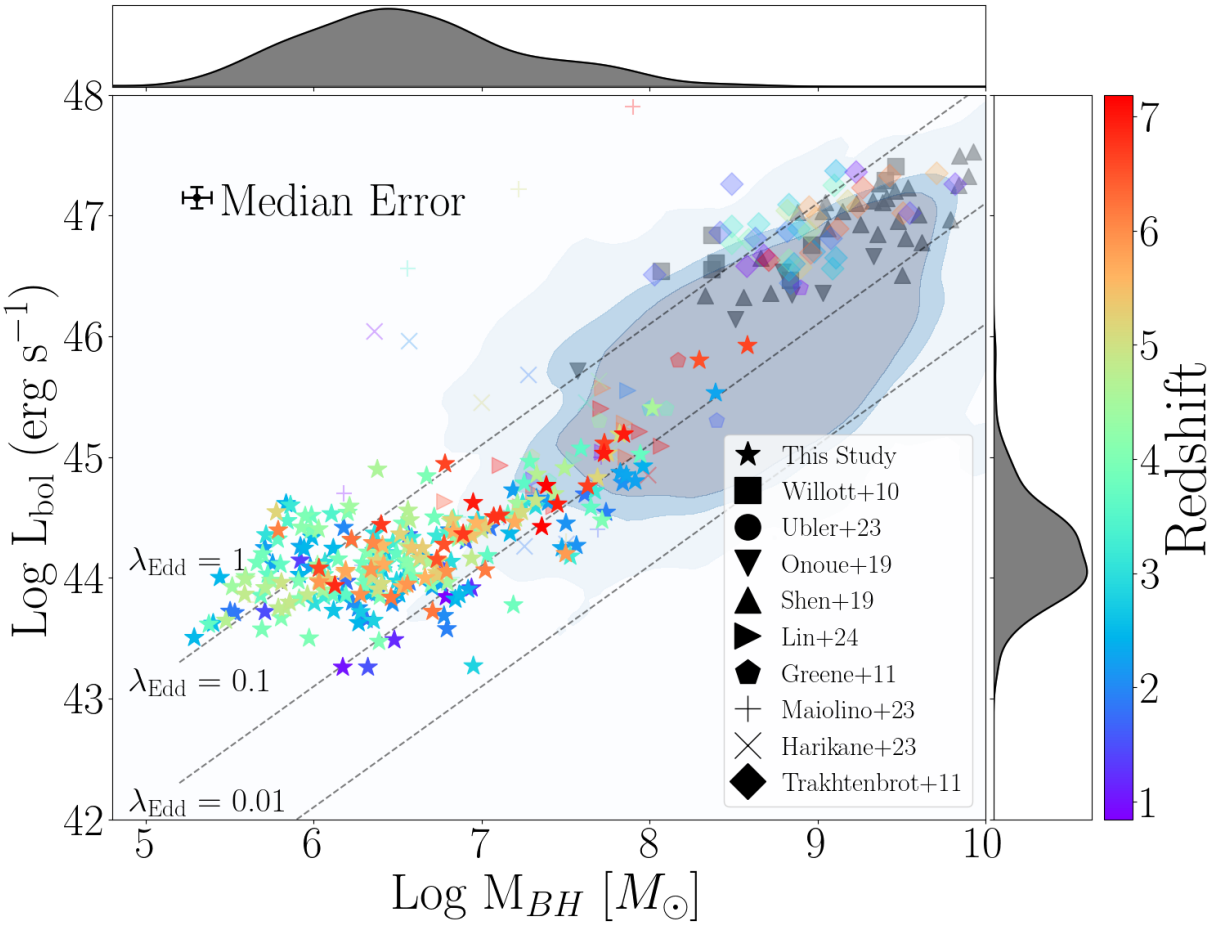


**Figure 3.** Black hole mass ($M_{\rm BH}$) versus bolometric luminosity ($L_{\rm bol}$) for our AGN sample. Color of points indicate redshift. Symbols indicate AGNs from this study (⋆), Willott et al. (2010) $z \approx 6$) (■), Übler et al. (2023) $z \sim 5.5$) (●), Onoue et al. (2019) $6.1 \leq z \leq 6.7$ (▼), Shen et al. (2019) $z \geq 5.7$(▲), Lin et al. (2024) $4 \leq z \leq 5$ (▶), Greene et al. (2024) $z \geq 5$ (⌓), Maiolino et al. (2024) $4 \leq z \leq 11$ (+), Harikane et al. (2023) $4 \leq z \leq 7$ (×) , and Trakhtenbrot et al. (2011) $z \leq 4.8$ (⧫). Light gray points are studies from which the redshift of the objects is not provided. Contours show low-$z$ AGNs from redshifts 1 – 2 from Sloan Digital Sky Survey (SDSS) data release 16 (Wu & Shen 2022) and the dashed lines show the Eddington ratio ($\lambda_{\rm edd}$) of 0.01, 0.1 and 1.

more distant objects exhibited a higher $\lambda_{\rm edd}$ compared to those at $z \sim$ 0, however, it was unclear whether this was due to selection bias of brighter AGNs. Our thorough search of the JWST NIRspec archive and our larger BLAGN sample support the conclusion that $\lambda_{\rm edd}$ increases systematically with redshift to the earliest observable time, indicating more rapid black hole growth and accretion in the early universe (see Figure 5). In addition, we find that high-redshift AGNs are systematically lower in both black hole mass and luminosity than their local counterparts. In Figure 1, we also observe an increasing fraction of BLAGNs out to a redshift of $z \sim$ 7. This increasing fraction and elevated Eddington ratios imply that the observed AGN population at $z > 4$ may represent a distinct phase of black hole–galaxy co-evolution.

### 5.2. *Ionization Mechanisms of the Discovered BLAGNs*

Despite JWST's transformative observational capacity, reliably distinguishing AGN-driven and stellar photoionization in early galaxies remains challenging. The dominant ionization mechanism in a galaxy can be diagnosed using emission-line ratios, particularly [N II]/H$\alpha$, [O II]/H$\beta$ in a BPT diagram (Baldwin et al. 1981). However, at high redshift and low metallicity, theoretical models predict that weakened [N II] emission can cause AGN-powered systems to fall within star-forming regions of standard diagnostic diagrams (e.g., Übler et al. 2023; Arevalo Gonzalez et al. 2025). Consequently, commonly adopted methods such as BPT diagrams may not reliably identify the primary ionization source in early universe systems, highlighting the need for additional observations. In Figure 6, we show our BLAGNs in the BPT diagram when they have sufficient coverage to cal-

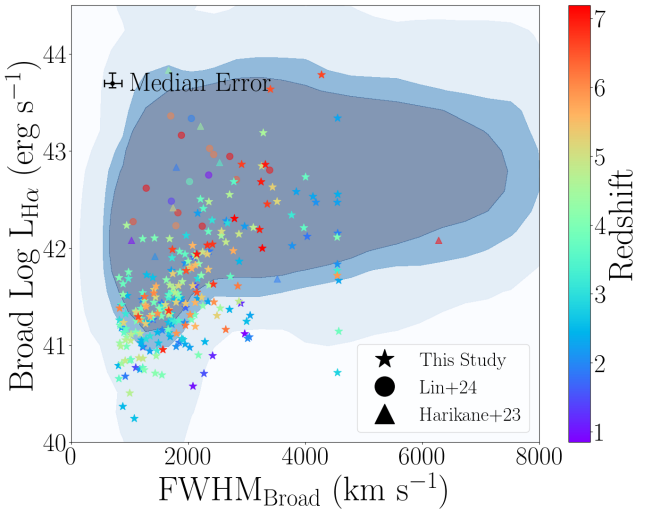


**Figure 4.** FWHM$_{H\alpha,broad}$ versus Log L$_{H\alpha,broad}$ for our sample of BLAGNs. The points are colored by redshift. Along with our BLAGNs, we overlay other BLAGNs found by Lin et al. (2024) (●), Greene et al. (2024) (▲), Maiolino et al. (2024) (⧫), Harikane et al. (2023) (⬠), Trakhtenbrot et al. (2011) (◀) , and Willott et al. (2010) (▶). BLAGNs identified in this study are shown as ⋆. Similarly as Figure 3, contours show low-$z$ AGNs from redshifts 1 – 2 (Wu & Shen 2022).

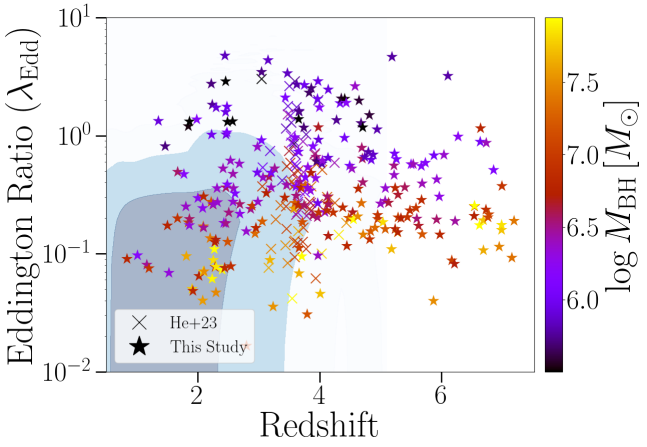


**Figure 5.** Eddington ratio ($\lambda_{edd}$) vs redshift for our sample. Color of points indicates black hole mass ($M_{BH}$). We also include BLAGNs found in He et al. (2024) as crosses. Similarly as Figure 4, we show the lower redshift AGNs from SDSS DR16 in different contours from Wu & Shen (2022).

culate the line ratios. We also overlay two curves that discriminate between galaxies dominated by AGNs and star-formation (Kewley et al. 2001; Kauffmann et al. 2003). We find that most of our sources fall into the AGN region in this diagram, while ∼ 15 others fall left of the curve of Kauffmann et al. (2003). One explanation for the latter is that they have lower metallicity that regular BLAGNs. Future dedicated studies can reveal if they do have relatively low metallicity.

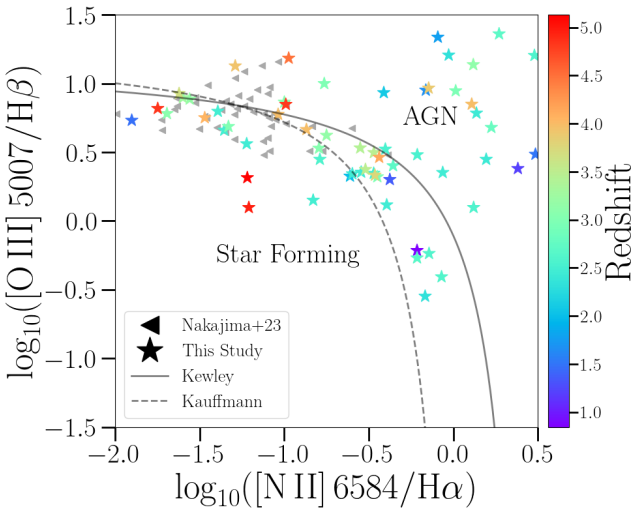


**Figure 6.** BPT diagram of our sample of BLAGNs. ⋆ show points from our study and ▶ are galaxies $z > 4$ found by Nakajima et al. (2023). The black solid and dashed curves show the limits between AGNs and starforming galaxies as found by Kewley et al. (2001) and Kauffmann et al. (2003).

### 5.3. *Caveats*

One limitation of our dataset is that the depths of the JWST observations vary across different surveys, which may lead to inhomogeneous BLAGN coverage. Future work would also benefit from additional high-resolution spectroscopy, as the majority of our BLAGNs (∼70%) are identified with medium-resolution data. Moreover, deeper spectroscopic observations are required to extend the accessible redshift range and to strengthen the robustness of broad-line identification. In particular, the S/N of the H$\beta$ line is often too low in early-universe sources ($z$> 6) to reliably detect the broad-line component, restricting the maximum redshift of our survey to $z\sim$ 7.2.

## 6. CONCLUSION

In this work, we conducted a comprehensive and systematic search for BLAGNs using the full spectroscopic range of JWST NIRSpec. From its medium- and high-resolution spectra, we identify 252 BLAGNs spanning redshifts of 0.8 – 7.2. This expanded sample offers insights into the growth and evolution of SMBHs in the early universe. Notably, high-redshift AGNs in our sample are characterized by systematically lower black hole masses and luminosities compared to local AGNs, yet they exhibit higher accretion efficiencies, indicating a

distinct evolutionary phase in black hole–galaxy coevolution at $z \gtrsim 4$. Our detection of a large population of faint, low-mass BLAGNs at high redshift helps bridge the observational gap between local SMBHs and the previously studied luminous quasars at high-redshift, providing a more complete view of AGN demographics in the early Universe.

C.B. acknowledges the Research Experiences in Astronomy at CIERA for High School Students (REACH) program, which initiated this project idea, and thanks J. Formato for helpful discussions. X.X. acknowledges the fellowship funding from Center for Interdisciplinary Exploration and Research in Astrophysics (CIERA), Northwestern University.

The data products presented here were retrieved from the Dawn JWST Archive (DJA). DJA is an initiative of the Cosmic Dawn Center (DAWN), which is funded by the Danish National Research Foundation under grant DNRF140.

The authors have used ChatGPT (OpenAI, 2023; https://chat.openai.com/chat to check coding syntax, and to check grammar in writing.

**Table 1**. Broad-line AGN Properties in Our Sample

| Object ID | R.A. | Decl. | $z$ | $\mathrm{FWHM_{H\alpha,broad}}$ | $\mathrm{Log}(M_{\mathrm{BH}})$ | $\mathrm{Log}(L_{\mathrm{bol}})$ | $\lambda_{\mathrm{edd}}$ | Grating |
|---|---|---|---|---|---|---|---|---|
| | | | | (km s$^{-1}$) | ($M_\odot$) | (erg s$^{-1}$) | | |
| GDN_4762_16620 | 189.071156 | 62.169815 | 0.8451 | $2960^{+240}_{-190}$ | $6.79^{+0.0158}_{-0.0165}$ | $43.8^{+0.010}_{-0.010}$ | $0.0902^{+0.0016}_{-0.00}$ | G140M |
| JADES_1181_25055 | 189.160382 | 62.227502 | 1.0169 | $2080^{+210}_{-190}$ | $6.17^{+0.0387}_{-0.0408}$ | $43.3^{+0.0178}_{-0.0192}$ | $0.0968^{+0.0035}_{-0.00}$ | G140M |
| SUSPENSE_2110_130040 | 150.527420 | 2.476694 | 1.1701 | $2410^{+220}_{-170}$ | $6.48^{+0.0378}_{-0.0312}$ | $43.5^{+0.0152}_{-0.0146}$ | $0.0805^{+0.0021}_{-0.00}$ | G140M |
| SUSPENSE_2110_128452 | 150.502426 | 2.450619 | 1.2054 | $2900^{+680}_{-290}$ | $6.94^{+0.0143}_{-0.0123}$ | $43.9^{+0.0232}_{-0.0129}$ | $0.0751^{+0.0023}_{-0.00}$ | G140M |
| JADES_1181_64818 | 189.026770 | 62.289835 | 1.3597 | $1220^{+120}_{-120}$ | $5.92^{+0.0269}_{-0.0382}$ | $44.1^{+0.010}_{-0.010}$ | $1.3314^{+0.0770}_{-0.08}$ | G140M |
| JADES_1180_44271 | 53.121652 | -27.737087 | 1.4704 | $1100^{+80}_{-90}$ | $5.71^{+0.0253}_{-0.0375}$ | $43.7^{+0.010}_{-0.0156}$ | $0.8128^{+0.0286}_{-0.05}$ | G140M |
| SUSPENSE_2110_130647 | 150.486252 | 2.486455 | 1.5078 | $2120^{+40}_{-60}$ | $6.76^{+0.0102}_{-0.0148}$ | $44.1^{+0.010}_{-0.010}$ | $0.1729^{+0.0017}_{-0.00}$ | G140M |
| EXCELS_3543_69759 | 34.348536 | -5.206934 | 1.5326 | $2270^{+480}_{-400}$ | $6.32^{+0.0484}_{-0.0468}$ | $43.3^{+0.0309}_{-0.010}$ | $0.0687^{+0.0044}_{-0.00}$ | G140M |
| GOODSN_1211_1795 | 189.066844 | 62.185505 | 1.6727 | $2090^{+190}_{-190}$ | $6.91^{+0.0197}_{-0.0165}$ | $44.3^{+0.0151}_{-0.02}$ | $0.1990^{+0.0053}_{-0.010}$ | G140M |
| JADES_1181_23924 | 189.032050 | 62.250886 | 1.6755 | $1950^{+150}_{-130}$ | $6.56^{+0.0264}_{-0.0389}$ | $44.4^{+0.010}_{-0.0102}$ | $0.4933^{+0.0256}_{-0.03}$ | G235H |
| JADES_1181_34145 | 189.121246 | 62.314985 | 1.7779 | $1400^{+110}_{-70}$ | $6.2^{+0.0161}_{-0.0165}$ | $44.0^{+0.010}_{-0.012}$ | $0.4718^{+0.0105}_{-0.010}$ | G235H |
| GOODSN_1211_4319 | 189.270307 | 62.267102 | 1.8097 | $1550^{+360}_{-580}$ | $6.38^{+0.0537}_{-0.0504}$ | $43.9^{+0.061}_{-0.010}$ | $0.2508^{+0.0208}_{-0.02}$ | G235H |
| EXCELS_3543_102901 | 34.379313 | -5.156950 | 1.8180 | $4030^{+110}_{-90}$ | $7.61^{+0.010}_{-0.010}$ | $44.7^{+0.010}_{-0.010}$ | $0.0951^{+0.0006}_{-0.00}$ | G235H |
| MACS1149_2758_150471 | 177.425171 | 22.465952 | 1.8498 | $2360^{+30}_{-30}$ | $7.05^{+0.010}_{-0.010}$ | $44.4^{+0.010}_{-0.010}$ | $0.1838^{+0.0008}_{-0.00}$ | G235H |
| BLUEJAY_1810_7185 | 150.105835 | 2.251845 | 1.8502 | $2620^{+1910}_{-2170}$ | $5.53^{+0.0636}_{-0.0304}$ | $43.7^{+0.010}_{-0.010}$ | $1.2012^{+0.1905}_{-0.09}$ | G235H |
| BLUEJAY_1810_19572 | 150.133196 | 2.378721 | 1.8673 | $1840^{+220}_{-200}$ | $6.31^{+0.0322}_{-0.0315}$ | $43.7^{+0.017}_{-0.0169}$ | $0.1739^{+0.0051}_{-0.00}$ | G235H |
| GTO_1214_2937 | 150.186564 | 2.455311 | 1.8676 | $1890^{+350}_{-260}$ | $6.57^{+0.0422}_{-0.0412}$ | $44.0^{+0.0189}_{-0.0244}$ | $0.1964^{+0.0090}_{-0.010}$ | G235H |
| BLUEJAY_1810_8500 | 150.083479 | 2.266050 | 1.8693 | $1280^{+110}_{-100}$ | $5.5^{+0.0289}_{-0.0306}$ | $43.7^{+0.0101}_{-0.0123}$ | $1.3176^{+0.0605}_{-0.05}$ | G235M |
| GTO_1215_4250 | 34.423424 | -5.271182 | 1.9116 | $4550^{+10}_{-200}$ | $7.74^{+0.0125}_{-0.0125}$ | $44.5^{+0.010}_{-0.010}$ | $0.0502^{+0.0005}_{-0.00}$ | G235M |
| BLUEJAY_1810_16419 | 150.095610 | 2.350069 | 1.9257 | $3040^{+540}_{-420}$ | $6.79^{+0.0364}_{-0.0383}$ | $43.6^{+0.0201}_{-0.010}$ | $0.0483^{+0.0027}_{-0.00}$ | G235M |
| JADES_1181_26194 | 189.171754 | 62.237978 | 1.9881 | $1210^{+560}_{-380}$ | $6.18^{+0.0308}_{-0.044}$ | $44.4^{+0.0108}_{-0.0129}$ | $1.3711^{+0.0711}_{-0.06}$ | G235M |
| BLUEJAY_1810_18688 | 150.133502 | 2.370408 | 2.0070 | $1550^{+240}_{-240}$ | $6.23^{+0.0363}_{-0.0476}$ | $43.8^{+0.0193}_{-0.0281}$ | $0.2957^{+0.0114}_{-0.010}$ | G235M |
| CEERS_1345_2904 | 215.048077 | 52.968341 | 2.0250 | $3010^{+590}_{-450}$ | $6.78^{+0.0562}_{-0.0581}$ | $43.7^{+0.017}_{-0.019}$ | $0.0646^{+0.0022}_{-0.00}$ | G235M |

**Table 1 – Cont.**

| Object ID | R.A. | Decl. | $z$ | $\mathrm{FWHM}_{\mathrm{H}\alpha,\mathrm{broad}}$ | $\mathrm{Log}(M_{\mathrm{BH}})$ | $\mathrm{Log}(\mathrm{L}_{\mathrm{bol}})$ | $\lambda_{\mathrm{edd}}$ | Grating |
|---|---|---|---|---|---|---|---|---|
| | | | | (km s$^{-1}$) | ($M_{\odot}$) | (erg s$^{-1}$) | | |
| BLUEJAY_1810_18668 | 150.129272 | 2.369564 | 2.0856 | $1790^{+160}_{-160}$ | $6.26^{+0.0332}_{-0.0442}$ | $43.8^{+0.0121}_{-0.015}$ | $0.2429^{+0.0096}_{-0.010}$ | G235M |
| BLUEJAY_1810_18977 | 150.146497 | 2.372308 | 2.0861 | $4550^{+10}_{-200}$ | $7.56^{+0.010}_{-0.010}$ | $44.3^{+0.010}_{-0.010}$ | $0.0400^{+0.0003}_{-0.00}$ | G235M |
| BLUEJAY_1810_12020 | 150.074554 | 2.301999 | 2.0934 | $4180^{+50}_{-70}$ | $7.84^{+0.010}_{-0.010}$ | $44.8^{+0.010}_{-0.010}$ | $0.0704^{+0.0003}_{-0.00}$ | G235M |
| BLUEJAY_1810_11337 | 150.119519 | 2.295778 | 2.0950 | $2650^{+30}_{-20}$ | $7.33^{+0.010}_{-0.010}$ | $44.7^{+0.010}_{-0.010}$ | $0.1701^{+0.0006}_{-0.00}$ | G235M |
| COSMOS_1879_2342 | 150.121785 | 2.213211 | 2.0986 | $1940^{+70}_{-90}$ | $6.47^{+0.0134}_{-0.0168}$ | $43.8^{+0.010}_{-0.010}$ | $0.1663^{+0.0022}_{-0.00}$ | G235M |
| BLUEJAY_1810_10314 | 150.085725 | 2.285124 | 2.0996 | $1940^{+20}_{-4080}$ | $6.81^{+0.82}_{-0.010}$ | $44.4^{+0.209}_{-0.010}$ | $0.3054^{+1.0732}_{-0.57}$ | G235M |
| GTO_1214_1158 | 150.132576 | 2.212071 | 2.1083 | $3770^{+830}_{-900}$ | $7.5^{+0.0426}_{-0.0455}$ | $44.5^{+0.0154}_{-0.0183}$ | $0.0707^{+0.0030}_{-0.00}$ | G235M |
| GTO_1215_4909 | 34.373619 | -5.185003 | 2.2078 | $2960^{+100}_{-100}$ | $7.4^{+0.010}_{-0.010}$ | $44.6^{+0.010}_{-0.010}$ | $0.1351^{+0.0011}_{-0.00}$ | G235M |
| GDS_1207_209962 | 53.131145 | -27.773187 | 2.2245 | $2160^{+20}_{-20}$ | $7.19^{+0.010}_{-0.010}$ | $44.7^{+0.010}_{-0.010}$ | $0.2746^{+0.0014}_{-0.00}$ | G235M |
| CECILIA_2593_25 | 356.637130 | 12.803911 | 2.2265 | $1050^{+40}_{-20}$ | $5.71^{+0.010}_{-0.010}$ | $44.2^{+0.010}_{-0.010}$ | $2.7509^{+0.0320}_{-0.04}$ | G235M |
| JADES_1181_27887 | 189.150275 | 62.249733 | 2.2313 | $1340^{+160}_{-150}$ | $5.98^{+0.0444}_{-0.0551}$ | $44.1^{+0.010}_{-0.0103}$ | $1.0199^{+0.0993}_{-0.09}$ | G235M |
| GOODSN_1211_4151 | 189.324563 | 62.315454 | 2.2409 | $4550^{+10}_{-200}$ | $7.91^{+0.010}_{-0.010}$ | $44.8^{+0.010}_{-0.010}$ | $0.0612^{+0.0003}_{-0.00}$ | G235M |
| CECILIA_2593_29 | 356.621640 | 12.817598 | 2.2427 | $1170^{+140}_{-240}$ | $5.75^{+0.0167}_{-0.036}$ | $44.1^{+0.010}_{-0.010}$ | $1.8283^{+0.0670}_{-0.13}$ | G235M |
| GTO_1215_3088 | 34.412371 | -5.267760 | 2.2553 | $1710^{+570}_{-300}$ | $6.65^{+0.0379}_{-0.0511}$ | $44.2^{+0.041}_{-0.0211}$ | $0.2605^{+0.0233}_{-0.02}$ | G235M |
| VALENTINO_3567_55536 | 34.450763 | -5.127912 | 2.2558 | $2020^{+410}_{-250}$ | $6.37^{+0.0367}_{-0.0475}$ | $43.9^{+0.0118}_{-0.0117}$ | $0.2622^{+0.0127}_{-0.010}$ | G235M |
| JADES_1181_28074 | 189.064589 | 62.273815 | 2.2600 | $3850^{+30}_{-20}$ | $7.83^{+0.010}_{-0.010}$ | $44.9^{+0.010}_{-0.010}$ | $0.0881^{+0.0003}_{-0.00}$ | G235M |
| LYC22_1869_4096 | 334.251380 | 0.332309 | 2.2762 | $4550^{+10}_{-200}$ | $8.39^{+0.010}_{-0.010}$ | $45.5^{+0.010}_{-0.010}$ | $0.1091^{+0.0003}_{-0.00}$ | G235M |
| VALENTINO_3567_71 | 34.761581 | -5.361252 | 2.2848 | $2340^{+90}_{-250}$ | $6.76^{+0.010}_{-0.0319}$ | $44.0^{+0.010}_{-0.0888}$ | $0.1252^{+0.0019}_{-0.010}$ | G235M |
| VALENTINO_3567_40904 | 34.408978 | -5.148414 | 2.2903 | $3060^{+120}_{-3960}$ | $6.92^{+0.977}_{-0.010}$ | $43.9^{+0.0131}_{-0.010}$ | $0.0770^{+0.4564}_{-0.25}$ | G235M |
| AURORA_1914_5469 | 150.179276 | 2.233684 | 2.2997 | $2160^{+40}_{-40}$ | $6.7^{+0.010}_{-0.010}$ | $43.9^{+0.010}_{-0.010}$ | $0.1312^{+0.0018}_{-0.00}$ | G235M |
| GTO_1215_3470 | 34.512380 | -5.189235 | 2.3026 | $4570^{+10}_{-690}$ | $7.48^{+0.0329}_{-0.029}$ | $44.2^{+0.010}_{-0.010}$ | $0.0468^{+0.0006}_{-0.00}$ | G235M |
| GOODSN_1211_2460 | 189.427236 | 62.303289 | 2.3056 | $4130^{+190}_{-160}$ | $7.86^{+0.010}_{-0.010}$ | $44.9^{+0.010}_{-0.010}$ | $0.0774^{+0.0006}_{-0.00}$ | G235M |
| COSMOS_1879_1295 | 150.125800 | 2.199290 | 2.3057 | $1220^{+70}_{-90}$ | $5.92^{+0.0253}_{-0.0225}$ | $44.3^{+0.010}_{-0.010}$ | $1.7305^{+0.1004}_{-0.07}$ | G235M |
| JADES_1181_29711 | 189.196910 | 62.284104 | 2.3204 | $1720^{+210}_{-170}$ | $6.35^{+0.0275}_{-0.0255}$ | $44.0^{+0.010}_{-0.0104}$ | $0.3584^{+0.0147}_{-0.010}$ | G235M |
| GDS_1671_37005 | 53.154439 | -27.738678 | 2.3277 | $1940^{+170}_{-120}$ | $6.35^{+0.048}_{-0.0319}$ | $43.9^{+0.0111}_{-0.010}$ | $0.2726^{+0.0221}_{-0.010}$ | G235M |
| CANTALUPO_1835_2044 | 10.393484 | -49.562990 | 2.4047 | $4550^{+10}_{-10}$ | $7.96^{+0.010}_{-0.010}$ | $44.9^{+0.010}_{-0.010}$ | $0.0729^{+0.0001}_{-0.00}$ | G235M |
| VALENTINO_3567_3285 | 36.736799 | -4.547720 | 2.4193 | $1450^{+140}_{-150}$ | $6.42^{+0.0222}_{-0.0305}$ | $44.2^{+0.0133}_{-0.0143}$ | $0.5268^{+0.0201}_{-0.02}$ | G235M |
| VALENTINO_3567_5276 | 149.949929 | 2.079299 | 2.4325 | $1690^{+360}_{-320}$ | $6.27^{+0.0646}_{-0.0742}$ | $43.6^{+0.0426}_{-0.0688}$ | $0.1820^{+0.0128}_{-0.010}$ | G235M |
| BLUEJAY_1810_11142 | 150.073292 | 2.293290 | 2.4465 | $2700^{+170}_{-140}$ | $6.84^{+0.0189}_{-0.0215}$ | $43.8^{+0.010}_{-0.010}$ | $0.0757^{+0.0020}_{-0.00}$ | G235M |
| CECILIA_2593_4 | 356.614369 | 12.786432 | 2.4498 | $1050^{+10}_{-30}$ | $5.84^{+0.0263}_{-0.016}$ | $44.6^{+0.010}_{-0.010}$ | $4.7643^{+0.2747}_{-0.18}$ | G235M |
| BLUEJAY_1810_12148 | 150.118698 | 2.302685 | 2.4612 | $1200^{+80}_{-110}$ | $5.94^{+0.0227}_{-0.0292}$ | $44.2^{+0.010}_{-0.010}$ | $1.5871^{+0.0724}_{-0.10}$ | G235M |
| VALENTINO_3567_54545 | 150.108418 | 2.378934 | 2.4616 | $1030^{+110}_{-110}$ | $5.44^{+0.0296}_{-0.0426}$ | $44.0^{+0.010}_{-0.010}$ | $2.8851^{+0.1573}_{-0.18}$ | G235M |
| BLUEJAY_1810_19705 | 150.107752 | 2.379484 | 2.4650 | $2280^{+280}_{-180}$ | $6.51^{+0.0378}_{-0.0291}$ | $43.9^{+0.010}_{-0.010}$ | $0.1808^{+0.0089}_{-0.00}$ | G235M |
| VALENTINO_3567_54546 | 150.107754 | 2.379469 | 2.4669 | $1870^{+80}_{-100}$ | $6.58^{+0.0146}_{-0.0136}$ | $44.2^{+0.010}_{-0.010}$ | $0.3636^{+0.0071}_{-0.010}$ | G235M |
| BLUEJAY_1810_19891 | 150.086225 | 2.381412 | 2.4675 | $1190^{+210}_{-140}$ | $5.92^{+0.0363}_{-0.0497}$ | $44.0^{+0.0121}_{-0.0133}$ | $1.0231^{+0.0701}_{-0.06}$ | G235M |
| GOODSN_1211_5243 | 189.154664 | 62.274602 | 2.4835 | $1010^{+320}_{-150}$ | $5.99^{+0.0348}_{-0.0418}$ | $44.3^{+0.0164}_{-0.0196}$ | $1.7602^{+0.1129}_{-0.10}$ | G235M |
| AURORA_1914_26798 | 189.154584 | 62.274625 | 2.4836 | $1300^{+90}_{-60}$ | $6.12^{+0.0108}_{-0.0139}$ | $44.2^{+0.010}_{-0.010}$ | $1.0639^{+0.0203}_{-0.02}$ | G235M |
| VALENTINO_3567_136272 | 34.452493 | -5.154707 | 2.4893 | $1470^{+100}_{-100}$ | $6.17^{+0.0108}_{-0.0147}$ | $43.9^{+0.010}_{-0.010}$ | $0.3854^{+0.0061}_{-0.00}$ | G235M |
| MACS1149_2758_150337 | 177.468506 | 22.514523 | 2.4919 | $1060^{+1150}_{-250}$ | $5.29^{+0.0373}_{-0.0452}$ | $43.5^{+0.0177}_{-0.0164}$ | $1.3078^{+0.1336}_{-0.08}$ | G235M |
| BLUEJAY_1810_8280 | 150.086472 | 2.264299 | 2.4943 | $2870^{+80}_{-80}$ | $7.17^{+0.010}_{-0.010}$ | $44.4^{+0.010}_{-0.010}$ | $0.1259^{+0.0009}_{-0.00}$ | G235M |
| GTO_1213_9063 | 215.094680 | 52.998226 | 2.5131 | $1770^{+300}_{-250}$ | $6.52^{+0.0508}_{-0.0571}$ | $44.0^{+0.0335}_{-0.0345}$ | $0.2230^{+0.0126}_{-0.010}$ | G235M |
| VALENTINO_3567_24 | 34.778169 | -5.366900 | 2.5405 | $1290^{+100}_{-60}$ | $6.38^{+0.0112}_{-0.010}$ | $44.3^{+0.0146}_{-0.010}$ | $0.6143^{+0.0183}_{-0.010}$ | G235M |
| VALENTINO_3567_406 | 34.786143 | -5.335534 | 2.5471 | $3000^{+150}_{-130}$ | $6.87^{+0.0106}_{-0.0117}$ | $43.9^{+0.010}_{-0.010}$ | $0.0781^{+0.0009}_{-0.00}$ | G235M |
| MACS1149_2758_40151 | 177.425232 | 22.468645 | 2.5750 | $1080^{+130}_{-130}$ | $5.4^{+0.0329}_{-0.0391}$ | $43.6^{+0.010}_{-0.010}$ | $1.3218^{+0.1070}_{-0.10}$ | G235M |
| VALENTINO_3567_4301 | 36.725819 | -4.533482 | 2.5826 | $1390^{+110}_{-140}$ | $6.43^{+0.0251}_{-0.0173}$ | $44.2^{+0.0164}_{-0.0185}$ | $0.4746^{+0.0136}_{-0.02}$ | G235M |
| JADES_1180_107700 | 53.146178 | -27.779934 | 2.5830 | $1660^{+160}_{-170}$ | $6.33^{+0.0233}_{-0.0233}$ | $43.9^{+0.013}_{-0.0129}$ | $0.2756^{+0.0083}_{-0.010}$ | G235M |
| JADES_1180_5807 | 53.185848 | -27.810034 | 2.5913 | $1710^{+120}_{-120}$ | $6.41^{+0.0208}_{-0.0259}$ | $44.1^{+0.010}_{-0.0102}$ | $0.3583^{+0.0092}_{-0.010}$ | G235M |

**Table 1 – Cont.**

| Object ID | R.A. | Decl. | $z$ | $\mathrm{FWHM_{H\alpha,broad}}$ | $\mathrm{Log}(M_{\mathrm{BH}})$ | $\mathrm{Log}(\mathrm{L_{bol}})$ | $\lambda_{\mathrm{edd}}$ | Grating |
|---|---|---|---|---|---|---|---|---|
| | | | | (km s$^{-1}$) | ($M_{\odot}$) | (erg s$^{-1}$) | | |
| JADES_1286_37746 | 53.182003 | -27.814182 | 2.6151 | $1490^{+160}_{-140}$ | $6.12^{+0.0213}_{-0.0294}$ | $43.7^{+0.013}_{-0.014}$ | $0.3238^{+0.0099}_{-0.010}$ | G235M |
| BLUEJAY_1810_8002 | 150.119934 | 2.261021 | 2.6864 | $1910^{+230}_{-210}$ | $6.36^{+0.0374}_{-0.03}$ | $44.2^{+0.010}_{-0.010}$ | $0.5792^{+0.0471}_{-0.03}$ | G235M |
| GDS_1207_208030 | 53.180521 | -27.779717 | 2.6935 | $1820^{+90}_{-80}$ | $6.56^{+0.010}_{-0.010}$ | $44.1^{+0.010}_{-0.010}$ | $0.2627^{+0.0041}_{-0.00}$ | G235M |
| JADES_1180_6112 | 53.178704 | -27.802697 | 2.6948 | $1670^{+340}_{-260}$ | $6.28^{+0.0452}_{-0.0443}$ | $43.7^{+0.0267}_{-0.0256}$ | $0.2177^{+0.0109}_{-0.010}$ | G235M |
| COSMOS_4318_126981 | 150.461199 | 2.429556 | 2.8003 | $1890^{+220}_{-160}$ | $6.36^{+0.0272}_{-0.0248}$ | $43.6^{+0.0155}_{-0.0153}$ | $0.1547^{+0.0042}_{-0.00}$ | G235M |
| EXCELS_3543_98447 | 34.374528 | -5.163477 | 2.8037 | $4550^{+10}_{-270}$ | $6.95^{+0.102}_{-0.116}$ | $43.3^{+0.010}_{-0.0216}$ | $0.0165^{+0.0019}_{-0.00}$ | G235M |
| GDS_1207_201027 | 53.126930 | -27.804682 | 2.8720 | $1660^{+70}_{-60}$ | $6.49^{+0.017}_{-0.0125}$ | $44.0^{+0.0129}_{-0.015}$ | $0.2390^{+0.0044}_{-0.00}$ | G235M |
| VALENTINO_3567_44021 | 214.876286 | 52.852347 | 2.8968 | $1960^{+20}_{-30}$ | $6.98^{+0.010}_{-0.010}$ | $44.5^{+0.010}_{-0.010}$ | $0.2538^{+0.0016}_{-0.00}$ | G235M |
| JADES_1181_721 | 189.153759 | 62.222323 | 2.9436 | $2670^{+40}_{-30}$ | $7.32^{+0.010}_{-0.010}$ | $44.6^{+0.010}_{-0.010}$ | $0.1482^{+0.0007}_{-0.00}$ | G235M |
| JADES_1181_28428 | 189.235679 | 62.253620 | 2.9579 | $2160^{+90}_{-90}$ | $6.82^{+0.0145}_{-0.0128}$ | $44.1^{+0.010}_{-0.010}$ | $0.1651^{+0.0025}_{-0.00}$ | G235M |
| JADES_1181_23367 | 189.201153 | 62.248935 | 2.9800 | $1280^{+1230}_{-300}$ | $6.0^{+0.0381}_{-0.0524}$ | $43.8^{+0.0617}_{-0.0698}$ | $0.4867^{+0.0647}_{-0.06}$ | G235M |
| VALENTINO_3567_10480 | 149.416615 | 2.042305 | 2.9827 | $1540^{+120}_{-110}$ | $6.36^{+0.0175}_{-0.0256}$ | $44.4^{+0.010}_{-0.010}$ | $0.8038^{+0.0265}_{-0.03}$ | G235M |
| VALENTINO_3567_51372 | 150.072298 | 2.370851 | 2.9896 | $1720^{+100}_{-90}$ | $6.38^{+0.0111}_{-0.0102}$ | $43.9^{+0.010}_{-0.010}$ | $0.2755^{+0.0046}_{-0.00}$ | G235M |
| LYC22_1869_20013 | 334.283137 | 0.337929 | 3.0488 | $1340^{+150}_{-170}$ | $6.07^{+0.0125}_{-0.0173}$ | $44.1^{+0.010}_{-0.010}$ | $0.9137^{+0.0230}_{-0.03}$ | G235M |
| LYC22_1869_20081 | 334.275953 | 0.314617 | 3.0502 | $1010^{+70}_{-40}$ | $5.72^{+0.0127}_{-0.0116}$ | $44.4^{+0.010}_{-0.010}$ | $3.4637^{+0.1181}_{-0.09}$ | G235M |
| JADES_1180_197911 | 53.165314 | -27.814140 | 3.0622 | $2410^{+50}_{-50}$ | $7.24^{+0.010}_{-0.010}$ | $44.6^{+0.010}_{-0.010}$ | $0.1873^{+0.0020}_{-0.00}$ | G235M |
| LYC22_1869_2009 | 334.235371 | 0.333313 | 3.0743 | $1570^{+50}_{-40}$ | $6.36^{+0.010}_{-0.010}$ | $44.1^{+0.010}_{-0.010}$ | $0.4420^{+0.0032}_{-0.00}$ | G235M |
| JADES_1181_22456 | 189.035722 | 62.243154 | 3.1289 | $1720^{+110}_{-100}$ | $6.73^{+0.0173}_{-0.0154}$ | $44.3^{+0.0124}_{-0.0111}$ | $0.3260^{+0.0068}_{-0.010}$ | G235M |
| AURORA_1914_4740 | 150.158779 | 2.226062 | 3.1566 | $1300^{+50}_{-40}$ | $5.86^{+0.010}_{-0.010}$ | $44.6^{+0.010}_{-0.010}$ | $4.3604^{+0.0665}_{-0.07}$ | G395H |
| AURORA_1914_921842 | 189.197371 | 62.253779 | 3.1738 | $1820^{+50}_{-60}$ | $6.58^{+0.010}_{-0.010}$ | $44.3^{+0.010}_{-0.010}$ | $0.4471^{+0.0047}_{-0.00}$ | G395H |
| JADES_1180_7384 | 53.178503 | -27.784107 | 3.1882 | $3760^{+50}_{-80}$ | $7.67^{+0.010}_{-0.010}$ | $44.7^{+0.010}_{-0.010}$ | $0.0883^{+0.0004}_{-0.00}$ | G395H |
| VALENTINO_3567_45518 | 150.115564 | 2.353696 | 3.2079 | $1760^{+150}_{-160}$ | $6.39^{+0.026}_{-0.0293}$ | $44.1^{+0.010}_{-0.010}$ | $0.3637^{+0.0107}_{-0.010}$ | G395H |
| BLUEJAY_1810_17000 | 150.115551 | 2.353707 | 3.2093 | $1460^{+250}_{-190}$ | $6.06^{+0.0503}_{-0.0539}$ | $43.8^{+0.0122}_{-0.0122}$ | $0.4856^{+0.0365}_{-0.03}$ | G395H |
| VALENTINO_3567_40442 | 214.895613 | 52.856498 | 3.2396 | $4540^{+10}_{-200}$ | $7.53^{+0.0241}_{-0.0202}$ | $44.2^{+0.010}_{-0.010}$ | $0.0355^{+0.0009}_{-0.00}$ | G395M |
| BLUEJAY_1810_7102 | 150.089834 | 2.250410 | 3.2653 | $1660^{+60}_{-70}$ | $6.47^{+0.010}_{-0.010}$ | $44.3^{+0.010}_{-0.010}$ | $0.5272^{+0.0073}_{-0.010}$ | G395M |
| JADES_1181_53501 | 189.295056 | 62.193572 | 3.4304 | $1990^{+180}_{-130}$ | $6.8^{+0.0144}_{-0.0134}$ | $44.4^{+0.010}_{-0.010}$ | $0.2984^{+0.0066}_{-0.00}$ | G395M |
| VALENTINO_3567_53035 | 214.864145 | 52.866148 | 3.4393 | $1010^{+50}_{-40}$ | $6.11^{+0.010}_{-0.010}$ | $44.5^{+0.010}_{-0.010}$ | $2.1047^{+0.0262}_{-0.03}$ | G395M |
| AURORA_1914_6124 | 150.181709 | 2.239991 | 3.4592 | $1830^{+350}_{-370}$ | $6.43^{+0.0293}_{-0.0397}$ | $44.1^{+0.0102}_{-0.0186}$ | $0.3815^{+0.0137}_{-0.03}$ | G395M |
| JADES_1286_180575 | 53.085472 | -27.858170 | 3.4741 | $1010^{+720}_{-100}$ | $5.84^{+0.027}_{-0.0316}$ | $44.5^{+0.0192}_{-0.0109}$ | $3.3781^{+0.2162}_{-0.19}$ | G395M |
| J0226_3325_1884 | 36.530834 | 3.056698 | 3.5811 | $2780^{+50}_{-40}$ | $7.59^{+0.010}_{-0.010}$ | $45.1^{+0.010}_{-0.010}$ | $0.2407^{+0.0014}_{-0.00}$ | G395M |
| COSMOS_4318_126891 | 150.486200 | 2.427953 | 3.5949 | $2260^{+20}_{-20}$ | $7.25^{+0.010}_{-0.010}$ | $44.8^{+0.010}_{-0.010}$ | $0.2688^{+0.0013}_{-0.00}$ | G395M |
| JADES_1180_17341 | 53.087269 | -27.729623 | 3.5963 | $1220^{+1090}_{-340}$ | $6.23^{+0.0478}_{-0.0615}$ | $44.3^{+0.0311}_{-0.0199}$ | $0.9697^{+0.0842}_{-0.05}$ | G395M |
| RUBIES_4233_50522 | 214.855980 | 52.854661 | 3.6138 | $1380^{+310}_{-210}$ | $6.19^{+0.0484}_{-0.0611}$ | $43.9^{+0.0334}_{-0.0414}$ | $0.3704^{+0.0241}_{-0.02}$ | G395M |
| RUBIES_4233_150323 | 34.417822 | -5.134842 | 3.6178 | $1720^{+150}_{-130}$ | $6.54^{+0.0213}_{-0.0144}$ | $44.1^{+0.0232}_{-0.011}$ | $0.3090^{+0.0169}_{-0.010}$ | G395M |
| STARK_2478_16056 | 342.180171 | -44.560590 | 3.6266 | $1020^{+560}_{-430}$ | $5.79^{+0.0474}_{-0.0603}$ | $44.3^{+0.0161}_{-0.0136}$ | $2.7151^{+0.3376}_{-0.26}$ | G395M |
| RUBIES_4233_58237 | 214.850571 | 52.866030 | 3.6493 | $1940^{+60}_{-90}$ | $6.86^{+0.010}_{-0.010}$ | $44.4^{+0.010}_{-0.0103}$ | $0.2581^{+0.0038}_{-0.00}$ | G395M |
| RUBIES_4233_61627 | 34.238394 | -5.205775 | 3.6546 | $1200^{+240}_{-190}$ | $6.06^{+0.0386}_{-0.0346}$ | $44.0^{+0.02}_{-0.0195}$ | $0.7311^{+0.0495}_{-0.03}$ | G395M |
| MACS1149_2758_60003 | 177.464005 | 22.517816 | 3.6639 | $1220^{+150}_{-130}$ | $5.8^{+0.0244}_{-0.03}$ | $44.1^{+0.010}_{-0.010}$ | $1.6196^{+0.0852}_{-0.09}$ | G395M |
| RUBIES_4233_150987 | 34.279081 | -5.134019 | 3.6645 | $2720^{+500}_{-420}$ | $7.03^{+0.0366}_{-0.036}$ | $44.2^{+0.0121}_{-0.0118}$ | $0.1118^{+0.0041}_{-0.00}$ | G395M |
| RUBIES_4233_15825 | 215.079264 | 52.934252 | 3.6650 | $3970^{+180}_{-180}$ | $7.65^{+0.010}_{-0.010}$ | $44.6^{+0.010}_{-0.010}$ | $0.0681^{+0.0008}_{-0.00}$ | G395M |
| JADES_1181_2916 | 189.107739 | 62.269525 | 3.6653 | $1100^{+270}_{-140}$ | $5.73^{+0.0343}_{-0.0348}$ | $44.0^{+0.0151}_{-0.0145}$ | $1.5960^{+0.0965}_{-0.08}$ | G395M |
| GDN_4762_36344 | 189.149320 | 62.207477 | 3.6813 | $1660^{+140}_{-130}$ | $6.49^{+0.016}_{-0.0144}$ | $44.2^{+0.010}_{-0.010}$ | $0.4060^{+0.0072}_{-0.010}$ | G395M |
| MACS1149_1199_20024 | 177.424202 | 22.386257 | 3.6960 | $1850^{+80}_{-90}$ | $6.83^{+0.0108}_{-0.010}$ | $44.5^{+0.010}_{-0.010}$ | $0.3608^{+0.0064}_{-0.00}$ | G395M |
| JADES_1180_209777 | 53.158471 | -27.774046 | 3.7099 | $4000^{+50}_{-50}$ | $7.94^{+0.010}_{-0.010}$ | $45.0^{+0.010}_{-0.010}$ | $0.0949^{+0.0004}_{-0.00}$ | G395M |
| VALENTINO_3567_20910 | 214.949018 | 52.851747 | 3.7197 | $2340^{+50}_{-60}$ | $7.16^{+0.010}_{-0.010}$ | $44.5^{+0.010}_{-0.010}$ | $0.1849^{+0.0012}_{-0.00}$ | G395M |
| GLIMPSE_9223_34789 | 342.233643 | -44.534100 | 3.7426 | $1020^{+460}_{-70}$ | $5.69^{+0.0118}_{-0.0122}$ | $43.9^{+0.0167}_{-0.010}$ | $1.1703^{+0.0428}_{-0.02}$ | G395M |
| GLIMPSE_9223_43084 | 342.233398 | -44.539059 | 3.7479 | $1830^{+50}_{-40}$ | $6.57^{+0.010}_{-0.010}$ | $44.1^{+0.010}_{-0.010}$ | $0.2577^{+0.0019}_{-0.00}$ | G395M |

**Table 1 – Cont.**

| Object ID | R.A. | Decl. | $z$ | $\mathrm{FWHM_{H\alpha,broad}}$ | $\mathrm{Log}(M_{\mathrm{BH}})$ | $\mathrm{Log}(\mathrm{L_{bol}})$ | $\lambda_{\mathrm{edd}}$ | Grating |
|---|---|---|---|---|---|---|---|---|
| | | | | (km s$^{-1}$) | ($M_{\odot}$) | (erg s$^{-1}$) | | |
| VALENTINO_3567_217057 | 149.425650 | 2.060945 | 3.7518 | $1030^{+30}_{-20}$ | $5.99^{+0.010}_{-0.010}$ | $44.5^{+0.010}_{-0.010}$ | $2.6850^{+0.0349}_{-0.04}$ | G395M |
| EXCELS_3543_67887 | 34.368747 | -5.214285 | 3.7650 | $2210^{+30}_{-30}$ | $7.29^{+0.010}_{-0.010}$ | $45.0^{+0.010}_{-0.010}$ | $0.3768^{+0.0025}_{-0.00}$ | G395M |
| VALENTINO_3567_1546 | 149.419071 | 2.017789 | 3.7675 | $1190^{+370}_{-280}$ | $6.11^{+0.0624}_{-0.109}$ | $43.9^{+0.0637}_{-0.0594}$ | $0.4435^{+0.0365}_{-0.04}$ | G395M |
| EXCELS_3543_34495 | 34.289463 | -5.269810 | 3.7976 | $4570^{+140}_{-610}$ | $7.19^{+0.0312}_{-0.0295}$ | $43.8^{+0.010}_{-0.010}$ | $0.0306^{+0.0006}_{-0.00}$ | G395M |
| RUBIES_4233_10036 | 34.381671 | -5.303742 | 3.8052 | $1510^{+180}_{-220}$ | $6.31^{+0.0291}_{-0.0224}$ | $44.0^{+0.0144}_{-0.012}$ | $0.3614^{+0.0127}_{-0.010}$ | G395M |
| EXCELS_3543_51825 | 34.360275 | -5.240628 | 3.8088 | $1650^{+400}_{-150}$ | $6.29^{+0.0844}_{-0.0889}$ | $44.1^{+0.0236}_{-0.0296}$ | $0.5400^{+0.5163}_{-0.21}$ | G395M |
| JADES_1286_179198 | 53.088977 | -27.860695 | 3.8299 | $1050^{+110}_{-120}$ | $5.66^{+0.025}_{-0.0279}$ | $44.1^{+0.010}_{-0.010}$ | $2.3138^{+0.1074}_{-0.11}$ | G395M |
| RUBIES_4233_37032 | 214.849388 | 52.811824 | 3.8515 | $1410^{+290}_{-160}$ | $6.3^{+0.0216}_{-0.0221}$ | $43.9^{+0.0403}_{-0.0286}$ | $0.3429^{+0.0233}_{-0.02}$ | G395M |
| RUBIES_4233_45502 | 214.896493 | 52.870871 | 3.8609 | $1860^{+20}_{-3720}$ | $6.72^{+0.0421}_{-0.0483}$ | $44.5^{+0.010}_{-0.0305}$ | $0.4834^{+0.1300}_{-0.10}$ | G395M |
| RUBIES_4233_41926 | 214.929216 | 52.885041 | 3.8650 | $1030^{+390}_{-130}$ | $5.7^{+0.0307}_{-0.0319}$ | $44.2^{+0.0199}_{-0.0139}$ | $2.5256^{+0.2004}_{-0.12}$ | G395M |
| EXCELS_3543_112990 | 34.274454 | -5.143780 | 3.8906 | $2110^{+290}_{-270}$ | $6.59^{+0.0299}_{-0.0379}$ | $44.0^{+0.010}_{-0.0138}$ | $0.2108^{+0.0052}_{-0.010}$ | G395M |
| RUBIES_4233_25712 | 214.860745 | 52.796831 | 3.8918 | $1080^{+50}_{-50}$ | $6.14^{+0.010}_{-0.010}$ | $44.2^{+0.010}_{-0.010}$ | $0.8128^{+0.0092}_{-0.010}$ | G395M |
| JADES_1180_13329 | 53.139038 | -27.784433 | 3.9358 | $1540^{+290}_{-220}$ | $6.3^{+0.0382}_{-0.0393}$ | $44.0^{+0.0135}_{-0.0132}$ | $0.4362^{+0.0191}_{-0.010}$ | G395M |
| GTO_1215_3757 | 34.322542 | -5.171391 | 3.9423 | $1220^{+240}_{-230}$ | $6.53^{+0.0266}_{-0.0298}$ | $44.5^{+0.034}_{-0.010}$ | $0.6607^{+0.0374}_{-0.03}$ | G395M |
| RUBIES_4233_16053 | 34.367104 | -5.293524 | 3.9523 | $1040^{+190}_{-100}$ | $5.69^{+0.0353}_{-0.0422}$ | $43.6^{+0.0225}_{-0.027}$ | $0.6064^{+0.0303}_{-0.03}$ | G395M |
| RUBIES_4233_147412 | 34.360740 | -5.139000 | 3.9653 | $2050^{+680}_{-460}$ | $6.54^{+0.0363}_{-0.0279}$ | $43.9^{+0.0199}_{-0.0288}$ | $0.2032^{+0.0126}_{-0.010}$ | G395M |
| JADES_1181_2331 | 189.057303 | 62.270060 | 3.9664 | $1110^{+190}_{-130}$ | $5.98^{+0.0293}_{-0.0522}$ | $44.4^{+0.010}_{-0.010}$ | $2.0469^{+0.1204}_{-0.17}$ | G395M |
| RUBIES_4233_160366 | 34.202863 | -5.121150 | 3.9706 | $1550^{+780}_{-580}$ | $5.97^{+0.128}_{-0.178}$ | $43.5^{+0.0559}_{-0.112}$ | $0.2676^{+0.0475}_{-0.04}$ | G395M |
| EXCELS_3543_113667 | 34.242590 | -5.143077 | 3.9746 | $2170^{+120}_{-110}$ | $6.39^{+0.0215}_{-0.0258}$ | $43.5^{+0.0209}_{-0.024}$ | $0.0964^{+0.0044}_{-0.00}$ | G395M |
| VALENTINO_3567_793 | 34.757418 | -5.302532 | 3.9757 | $1030^{+40}_{-50}$ | $5.95^{+0.0119}_{-0.014}$ | $44.5^{+0.010}_{-0.010}$ | $2.8925^{+0.0661}_{-0.07}$ | G395M |
| RUBIES_4233_8895 | 34.363041 | -5.306108 | 3.9810 | $1420^{+150}_{-120}$ | $6.67^{+0.0213}_{-0.0167}$ | $44.8^{+0.010}_{-0.010}$ | $1.1773^{+0.0483}_{-0.03}$ | G395M |
| VALENTINO_3567_1369 | 149.430359 | 2.010774 | 3.9827 | $1100^{+580}_{-360}$ | $5.91^{+0.0307}_{-0.0488}$ | $44.0^{+0.0171}_{-0.0234}$ | $0.9237^{+0.0490}_{-0.04}$ | G395M |
| VALENTINO_3567_18 | 34.316190 | -5.051441 | 3.9856 | $2110^{+10}_{-4070}$ | $6.93^{+0.89}_{-0.010}$ | $44.4^{+0.010}_{-0.010}$ | $0.2234^{+0.8278}_{-1.02}$ | G395M |
| RUBIES_4233_30969 | 34.296356 | -5.268672 | 3.9989 | $1250^{+200}_{-200}$ | $6.2^{+0.0187}_{-0.0304}$ | $44.5^{+0.010}_{-0.0111}$ | $1.7362^{+0.0660}_{-0.10}$ | G395M |
| VALENTINO_3567_262 | 34.298697 | -4.989901 | 4.0116 | $4540^{+10}_{-200}$ | $7.72^{+0.010}_{-0.010}$ | $44.5^{+0.010}_{-0.010}$ | $0.0457^{+0.0007}_{-0.00}$ | G395M |
| GLASS_1324_160133 | 3.58027536 | -30.42440414 | 4.0116 | $750^{+30}_{-20}$ | $5.82^{+0.0109}_{-0.007}$ | $44.5^{+0.005}_{-0.005}$ | $4.091^{+0.059}_{-0.082}$ | G395H |
| JADES_1180_10013268 | 53.201828 | -27.820880 | 4.0395 | $1240^{+440}_{-180}$ | $5.81^{+0.0287}_{-0.0425}$ | $43.7^{+0.0139}_{-0.013}$ | $0.5783^{+0.0292}_{-0.03}$ | G395M |
| AURORA_1914_927605 | 189.151830 | 62.272228 | 4.0472 | $1500^{+130}_{-110}$ | $6.32^{+0.0131}_{-0.0162}$ | $44.2^{+0.010}_{-0.010}$ | $0.6152^{+0.0113}_{-0.010}$ | G395M |
| RUBIES_4233_119559 | 34.304860 | -5.177419 | 4.0885 | $1690^{+220}_{-210}$ | $6.39^{+0.05}_{-0.0477}$ | $43.8^{+0.0261}_{-0.0321}$ | $0.2250^{+0.0103}_{-0.010}$ | G395M |
| EXCELS_3543_42268 | 34.297511 | -5.257169 | 4.1204 | $2220^{+60}_{-60}$ | $6.86^{+0.010}_{-0.010}$ | $44.3^{+0.010}_{-0.010}$ | $0.2326^{+0.0018}_{-0.00}$ | G395M |
| RUBIES_4233_31747 | 34.223757 | -5.260245 | 4.1291 | $1620^{+70}_{-4030}$ | $6.55^{+0.848}_{-0.010}$ | $44.1^{+0.0747}_{-0.010}$ | $0.3047^{+2.7160}_{-2.43}$ | G395M |
| JADES_1181_73488 | 189.197396 | 62.177233 | 4.1325 | $2000^{+50}_{-50}$ | $6.84^{+0.010}_{-0.010}$ | $44.4^{+0.010}_{-0.010}$ | $0.2658^{+0.0016}_{-0.00}$ | G395M |
| GDN_2674_3761 | 189.259528 | 62.172083 | 4.1393 | $1430^{+350}_{-310}$ | $5.91^{+0.0326}_{-0.0404}$ | $43.8^{+0.010}_{-0.010}$ | $0.6491^{+0.0364}_{-0.04}$ | G395M |
| EXCELS_3543_89922 | 34.255946 | -5.177851 | 4.1427 | $880^{+80}_{-60}$ | $5.93^{+0.0203}_{-0.0182}$ | $44.4^{+0.010}_{-0.010}$ | $2.4580^{+0.0864}_{-0.07}$ | G395M |
| JADES_1181_72127 | 189.265718 | 62.168393 | 4.1438 | $2250^{+270}_{-210}$ | $6.7^{+0.0254}_{-0.0384}$ | $43.9^{+0.0144}_{-0.0182}$ | $0.1414^{+0.0041}_{-0.00}$ | G395M |
| RUBIES_4233_119957 | 34.268908 | -5.176722 | 4.1489 | $1820^{+140}_{-140}$ | $6.58^{+0.0144}_{-0.0155}$ | $44.1^{+0.010}_{-0.010}$ | $0.2609^{+0.0050}_{-0.00}$ | G395M |
| RUBIES_4233_28812 | 214.924149 | 52.849050 | 4.2246 | $2180^{+130}_{-100}$ | $6.91^{+0.010}_{-0.0115}$ | $44.4^{+0.010}_{-0.010}$ | $0.2232^{+0.0026}_{-0.00}$ | G395M |
| RUBIES_4233_41683 | 214.839934 | 52.820067 | 4.2792 | $1080^{+350}_{-200}$ | $5.75^{+0.0341}_{-0.061}$ | $44.0^{+0.018}_{-0.0243}$ | $1.3537^{+0.0800}_{-0.10}$ | G395M |
| GDN_4762_37583 | 189.096767 | 62.209854 | 4.3359 | $1100^{+170}_{-140}$ | $6.03^{+0.0287}_{-0.0276}$ | $44.4^{+0.010}_{-0.010}$ | $1.8828^{+0.1364}_{-0.09}$ | G395M |
| RUBIES_4233_54059 | 34.280915 | -5.220847 | 4.3567 | $1030^{+350}_{-170}$ | $5.59^{+0.048}_{-0.0591}$ | $44.0^{+0.0212}_{-0.0145}$ | $2.0645^{+0.2173}_{-0.14}$ | G395M |
| AURORA_1914_928583 | 189.124835 | 62.275492 | 4.3807 | $2350^{+180}_{-130}$ | $6.86^{+0.010}_{-0.0113}$ | $44.3^{+0.010}_{-0.010}$ | $0.2463^{+0.0031}_{-0.00}$ | G395M |
| JADES_1181_11836 | 189.220587 | 62.263675 | 4.4095 | $1450^{+200}_{-200}$ | $6.02^{+0.0236}_{-0.0282}$ | $44.1^{+0.010}_{-0.010}$ | $0.9571^{+0.0431}_{-0.05}$ | G395M |
| JADES_1181_28746 | 189.176078 | 62.256325 | 4.4126 | $860^{+280}_{-130}$ | $5.51^{+0.0296}_{-0.0379}$ | $43.9^{+0.0158}_{-0.0116}$ | $2.0495^{+0.1509}_{-0.11}$ | G395M |
| JADES_1180_16375 | 53.095744 | -27.774815 | 4.4374 | $1380^{+400}_{-420}$ | $6.21^{+0.0446}_{-0.0561}$ | $44.6^{+0.010}_{-0.0136}$ | $1.8975^{+0.1722}_{-0.17}$ | G395M |
| JADES_1181_53757 | 189.269778 | 62.194208 | 4.4482 | $2540^{+370}_{-270}$ | $6.8^{+0.0172}_{-0.017}$ | $44.0^{+0.0157}_{-0.0159}$ | $0.1162^{+0.0037}_{-0.00}$ | G395M |
| CEERS_1345_1244 | 215.240652 | 53.036041 | 4.4779 | $2560^{+90}_{-70}$ | $7.21^{+0.010}_{-0.010}$ | $44.6^{+0.010}_{-0.010}$ | $0.2007^{+0.0019}_{-0.00}$ | G395M |
| MACS1149_1199_80002 | 177.394550 | 22.394321 | 4.4944 | $1160^{+150}_{-400}$ | $6.05^{+0.0448}_{-0.0523}$ | $43.9^{+0.0298}_{-0.0499}$ | $0.5552^{+0.0304}_{-0.05}$ | G395M |

**Table 1 – Cont.**

| Object ID | R.A. | Decl. | $z$ | $\mathrm{FWHM}_{\mathrm{H}\alpha,\mathrm{broad}}$ | $\mathrm{Log}(M_{\mathrm{BH}})$ | $\mathrm{Log}(\mathrm{L}_{\mathrm{bol}})$ | $\lambda_{\mathrm{edd}}$ | Grating |
|---|---|---|---|---|---|---|---|---|
| | | | | (km s$^{-1}$) | ($M_{\odot}$) | (erg s$^{-1}$) | | |
| AURORA_1914_8769 | 150.175130 | 2.268880 | 4.5302 | $1630^{+100}_{-80}$ | $6.39^{+0.010}_{-0.010}$ | $44.2^{+0.010}_{-0.010}$ | $0.5263^{+0.0064}_{-0.010}$ | G395M |
| RUBIES_4233_29489 | 215.022071 | 52.920786 | 4.5434 | $1900^{+130}_{-180}$ | $6.68^{+0.025}_{-0.014}$ | $44.1^{+0.0174}_{-0.010}$ | $0.2239^{+0.0055}_{-0.00}$ | G395M |
| GTO_1215_1472 | 34.337315 | -5.143674 | 4.5563 | $3280^{+50}_{-50}$ | $8.02^{+0.010}_{-0.010}$ | $45.4^{+0.010}_{-0.010}$ | $0.1949^{+0.0010}_{-0.00}$ | G395M |
| GTO_1215_6001 | 34.364248 | -5.197730 | 4.5825 | $1150^{+590}_{-250}$ | $6.38^{+0.0207}_{-0.03}$ | $44.9^{+0.0196}_{-0.0124}$ | $2.6247^{+0.0935}_{-0.08}$ | G395M |
| VALENTINO_3567_51909 | 34.454931 | -5.132708 | 4.6262 | $2700^{+30}_{-30}$ | $7.49^{+0.010}_{-0.010}$ | $44.9^{+0.010}_{-0.010}$ | $0.2067^{+0.0009}_{-0.00}$ | G395M |
| GTO_1213_3848 | 215.034109 | 52.984404 | 4.6348 | $1680^{+390}_{-340}$ | $6.82^{+0.046}_{-0.0535}$ | $44.5^{+0.0418}_{-0.0217}$ | $0.3552^{+0.0265}_{-0.03}$ | G395M |
| GDS_1210_9515 | 53.132843 | -27.801854 | 4.6477 | $1090^{+370}_{-120}$ | $5.59^{+0.0196}_{-0.025}$ | $44.0^{+0.010}_{-0.010}$ | $1.9821^{+0.0588}_{-0.06}$ | G395M |
| JADES_1181_20621 | 189.122515 | 62.292850 | 4.6806 | $930^{+690}_{-140}$ | $5.71^{+0.024}_{-0.0414}$ | $43.9^{+0.0243}_{-0.0185}$ | $1.2762^{+0.0659}_{-0.06}$ | G395M |
| GTO_1215_4446 | 34.270712 | -5.217671 | 4.6867 | $2350^{+120}_{-120}$ | $7.33^{+0.010}_{-0.010}$ | $44.9^{+0.010}_{-0.010}$ | $0.2679^{+0.0030}_{-0.00}$ | G395M |
| MACS1149_2758_60001 | 177.465897 | 22.518972 | 4.6923 | $1770^{+50}_{-70}$ | $6.56^{+0.010}_{-0.010}$ | $44.6^{+0.010}_{-0.010}$ | $0.7893^{+0.0098}_{-0.010}$ | G395M |
| GOODSN_1211_2066 | 189.238138 | 62.136970 | 4.7017 | $1740^{+440}_{-350}$ | $6.57^{+0.0419}_{-0.0472}$ | $44.5^{+0.010}_{-0.010}$ | $0.6392^{+0.0405}_{-0.03}$ | G395M |
| MACS0416_4750_50001 | 64.022008 | -24.067001 | 4.7079 | $1030^{+280}_{-420}$ | $5.48^{+0.0324}_{-0.0294}$ | $43.6^{+0.0106}_{-0.0118}$ | $1.1745^{+0.0476}_{-0.04}$ | G395M |
| RUBIES_4233_42658 | 34.401816 | -5.250166 | 4.7100 | $1680^{+260}_{-210}$ | $6.56^{+0.0224}_{-0.0215}$ | $44.3^{+0.0105}_{-0.0101}$ | $0.4024^{+0.0093}_{-0.010}$ | G395M |
| RUBIES_4233_182791 | 34.213813 | -5.087050 | 4.7145 | $3110^{+90}_{-80}$ | $7.43^{+0.010}_{-0.010}$ | $44.7^{+0.010}_{-0.010}$ | $0.1450^{+0.0010}_{-0.00}$ | G395M |
| JADES_1286_172975 | 53.087730 | -27.871242 | 4.7417 | $1020^{+200}_{-140}$ | $5.83^{+0.0377}_{-0.0407}$ | $43.7^{+0.0159}_{-0.0176}$ | $0.6590^{+0.0234}_{-0.02}$ | G395M |
| EGS_4106_71365 | 214.895545 | 52.906722 | 4.8004 | $1010^{+200}_{-100}$ | $5.79^{+0.0267}_{-0.0299}$ | $43.8^{+0.0176}_{-0.0193}$ | $0.7263^{+0.0295}_{-0.03}$ | G395M |
| RUBIES_4233_48449 | 34.231608 | -5.230873 | 4.8174 | $1030^{+300}_{-230}$ | $5.59^{+0.068}_{-0.114}$ | $43.9^{+0.0195}_{-0.0328}$ | $1.4932^{+0.1966}_{-0.20}$ | G395M |
| JADES_1286_38562 | 53.135864 | -27.871645 | 4.8218 | $2870^{+240}_{-250}$ | $6.94^{+0.0285}_{-0.0324}$ | $44.2^{+0.010}_{-0.010}$ | $0.1322^{+0.0016}_{-0.00}$ | G395M |
| VALENTINO_3567_1552 | 149.412489 | 2.018099 | 4.8376 | $2640^{+100}_{-80}$ | $7.2^{+0.010}_{-0.010}$ | $44.5^{+0.010}_{-0.010}$ | $0.1546^{+0.0013}_{-0.00}$ | G395M |
| JADES_1181_39353 | 189.293952 | 62.153091 | 4.8475 | $1180^{+660}_{-190}$ | $5.96^{+0.0322}_{-0.0454}$ | $43.9^{+0.0205}_{-0.0344}$ | $0.6250^{+0.0294}_{-0.04}$ | G395M |
| RUBIES_4233_6411 | 215.109185 | 52.939770 | 4.8796 | $1220^{+160}_{-130}$ | $5.86^{+0.0279}_{-0.0489}$ | $43.8^{+0.0125}_{-0.02}$ | $0.6908^{+0.0306}_{-0.05}$ | G395M |
| J0910_2028_14324 | 137.714327 | -4.221305 | 4.9093 | $2860^{+70}_{-60}$ | $7.32^{+0.010}_{-0.010}$ | $44.6^{+0.010}_{-0.010}$ | $0.1659^{+0.0017}_{-0.00}$ | G395M |
| JADES_1180_13520 | 53.131565 | -27.809901 | 4.9441 | $1150^{+410}_{-240}$ | $5.81^{+0.042}_{-0.0577}$ | $44.0^{+0.0108}_{-0.0116}$ | $1.1296^{+0.0908}_{-0.08}$ | G395M |
| EGS_4106_51623 | 214.886818 | 52.855389 | 4.9528 | $2240^{+80}_{-60}$ | $7.0^{+0.010}_{-0.010}$ | $44.4^{+0.010}_{-0.010}$ | $0.1964^{+0.0028}_{-0.00}$ | G395M |
| RUBIES_4233_42232 | 214.886792 | 52.855381 | 4.9528 | $2130^{+130}_{-140}$ | $6.93^{+0.0115}_{-0.0138}$ | $44.4^{+0.010}_{-0.010}$ | $0.2124^{+0.0039}_{-0.00}$ | G395M |
| MACS0416_4750_60009 | 64.056234 | -24.113539 | 4.9992 | $1660^{+60}_{-80}$ | $6.38^{+0.010}_{-0.010}$ | $43.9^{+0.010}_{-0.010}$ | $0.2658^{+0.0030}_{-0.00}$ | G395M |
| JADES_1181_68797 | 189.229137 | 62.146190 | 5.0397 | $3250^{+60}_{-30}$ | $7.82^{+0.010}_{-0.010}$ | $45.2^{+0.010}_{-0.010}$ | $0.1850^{+0.0007}_{-0.00}$ | G395M |
| RUBIES_4233_166271 | 34.353256 | -5.112267 | 5.0758 | $1610^{+390}_{-360}$ | $6.4^{+0.0438}_{-0.0444}$ | $44.0^{+0.034}_{-0.0301}$ | $0.2796^{+0.0181}_{-0.02}$ | G395M |
| JADES_1286_159717 | 53.097528 | -27.901260 | 5.0774 | $2570^{+50}_{-40}$ | $7.24^{+0.010}_{-0.010}$ | $44.5^{+0.010}_{-0.010}$ | $0.1615^{+0.0008}_{-0.00}$ | G395M |
| RUBIES_4233_61496 | 214.972441 | 52.962192 | 5.0795 | $1440^{+180}_{-150}$ | $6.35^{+0.0261}_{-0.0222}$ | $44.0^{+0.0248}_{-0.018}$ | $0.3586^{+0.0163}_{-0.010}$ | G395M |
| VALENTINO_3567_44330 | 150.076721 | 2.350921 | 5.1308 | $1830^{+670}_{-390}$ | $6.63^{+0.0241}_{-0.028}$ | $44.2^{+0.0394}_{-0.0541}$ | $0.2703^{+0.0227}_{-0.02}$ | G395M |
| GDN_2674_14 | 189.199812 | 62.161474 | 5.1800 | $3520^{+60}_{-60}$ | $7.69^{+0.010}_{-0.010}$ | $44.8^{+0.010}_{-0.010}$ | $0.1092^{+0.0006}_{-0.00}$ | G395M |
| JADES_1181_78773 | 189.202942 | 62.204654 | 5.1876 | $890^{+220}_{-100}$ | $5.78^{+0.0156}_{-0.0282}$ | $44.5^{+0.010}_{-0.010}$ | $4.6524^{+0.1701}_{-0.24}$ | G395M |
| GDN_2674_32 | 189.265470 | 62.199359 | 5.2197 | $1790^{+220}_{-190}$ | $6.51^{+0.0188}_{-0.0184}$ | $44.4^{+0.010}_{-0.010}$ | $0.5579^{+0.0193}_{-0.010}$ | G395M |
| RUBIES_4233_148866 | 34.326433 | -5.137382 | 5.2226 | $1410^{+230}_{-160}$ | $6.37^{+0.0242}_{-0.0296}$ | $44.1^{+0.0165}_{-0.0171}$ | $0.4639^{+0.0157}_{-0.010}$ | G395M |
| JADES_1181_77652 | 189.293228 | 62.199003 | 5.2286 | $1110^{+170}_{-150}$ | $6.03^{+0.0315}_{-0.0304}$ | $44.0^{+0.0142}_{-0.0133}$ | $0.7048^{+0.0225}_{-0.02}$ | G395M |
| CEERS_1345_2782 | 214.823453 | 52.830281 | 5.2390 | $2490^{+410}_{-500}$ | $6.73^{+0.0279}_{-0.0315}$ | $44.0^{+0.010}_{-0.010}$ | $0.1615^{+0.0042}_{-0.00}$ | G395M |
| RUBIES_4233_50052 | 214.823454 | 52.830277 | 5.2394 | $2020^{+100}_{-100}$ | $6.82^{+0.010}_{-0.010}$ | $44.5^{+0.010}_{-0.010}$ | $0.3601^{+0.0052}_{-0.00}$ | G395M |
| RUBIES_4233_13872 | 215.132933 | 52.970705 | 5.2611 | $1270^{+1440}_{-410}$ | $6.08^{+0.0389}_{-0.055}$ | $44.0^{+0.0374}_{-0.0202}$ | $0.6320^{+0.0487}_{-0.03}$ | G395M |
| RUBIES_4233_42046 | 214.795368 | 52.788847 | 5.2772 | $3440^{+80}_{-50}$ | $7.75^{+0.010}_{-0.010}$ | $45.0^{+0.010}_{-0.010}$ | $0.1513^{+0.0009}_{-0.00}$ | G395M |
| RUBIES_4233_970351 | 34.261900 | -5.105205 | 5.2822 | $2230^{+650}_{-590}$ | $6.74^{+0.0438}_{-0.0424}$ | $44.0^{+0.0347}_{-0.0315}$ | $0.1519^{+0.0104}_{-0.010}$ | G395M |
| RUBIES_4233_926125 | 215.137081 | 52.988554 | 5.2858 | $1730^{+140}_{-110}$ | $6.65^{+0.0139}_{-0.0117}$ | $44.2^{+0.010}_{-0.010}$ | $0.3156^{+0.0059}_{-0.00}$ | G395M |
| RUBIES_4233_60935 | 214.923373 | 52.925593 | 5.2871 | $2330^{+120}_{-130}$ | $7.02^{+0.0112}_{-0.010}$ | $44.4^{+0.010}_{-0.010}$ | $0.2027^{+0.0034}_{-0.00}$ | G395M |
| MACS0416_4750_60003 | 64.052479 | -24.081456 | 5.3340 | $2080^{+40}_{-40}$ | $6.74^{+0.010}_{-0.010}$ | $44.1^{+0.010}_{-0.010}$ | $0.1998^{+0.0013}_{-0.00}$ | G395M |
| MACS1149_2758_40149 | 177.425964 | 22.468496 | 5.3971 | $1950^{+100}_{-80}$ | $6.58^{+0.010}_{-0.0124}$ | $44.2^{+0.010}_{-0.010}$ | $0.3653^{+0.0054}_{-0.010}$ | G395M |
| RUBIES_4233_29813 | 34.453355 | -5.270717 | 5.4399 | $2340^{+340}_{-350}$ | $6.94^{+0.0222}_{-0.0213}$ | $44.4^{+0.010}_{-0.010}$ | $0.2037^{+0.0042}_{-0.00}$ | G395M |
| JADES_1286_204851 | 53.138593 | -27.790253 | 5.4818 | $2120^{+100}_{-90}$ | $6.88^{+0.010}_{-0.010}$ | $44.3^{+0.010}_{-0.010}$ | $0.2324^{+0.0024}_{-0.00}$ | G395M |

**Table 1 – Cont.**

| Object ID | R.A. | Decl. | $z$ | $\mathrm{FWHM_{H\alpha,broad}}$ | $\mathrm{Log}(M_{\mathrm{BH}})$ | $\mathrm{Log}(L_{\mathrm{bol}})$ | $\lambda_{\mathrm{edd}}$ | Grating |
|---|---|---|---|---|---|---|---|---|
| | | | | (km s$^{-1}$) | ($M_\odot$) | (erg s$^{-1}$) | | |
| RUBIES_4233_17604 | 34.311488 | -5.290996 | 5.5002 | $1260^{+150}_{-110}$ | $6.19^{+0.023}_{-0.0239}$ | $44.0^{+0.010}_{-0.010}$ | $0.5719^{+0.0123}_{-0.010}$ | G395M |
| GDN_2674_934 | 189.261346 | 62.231967 | 5.5362 | $1670^{+160}_{-130}$ | $6.41^{+0.0164}_{-0.022}$ | $44.3^{+0.010}_{-0.010}$ | $0.5731^{+0.0160}_{-0.02}$ | G395M |
| RUBIES_4233_172350 | 34.368951 | -5.103941 | 5.5810 | $2070^{+120}_{-110}$ | $6.97^{+0.0108}_{-0.010}$ | $44.5^{+0.010}_{-0.010}$ | $0.2438^{+0.0043}_{-0.00}$ | G395M |
| JADES_1181_1093 | 189.179743 | 62.224629 | 5.5944 | $2120^{+470}_{-390}$ | $6.53^{+0.0293}_{-0.0362}$ | $43.9^{+0.011}_{-0.010}$ | $0.1978^{+0.0047}_{-0.00}$ | G395M |
| CEERS_1345_746 | 214.809142 | 52.868484 | 5.6231 | $2120^{+420}_{-390}$ | $6.66^{+0.0324}_{-0.0332}$ | $44.0^{+0.0249}_{-0.0379}$ | $0.1722^{+0.0093}_{-0.010}$ | G395M |
| RUBIES_4233_19521 | 34.383672 | -5.287732 | 5.6687 | $1340^{+430}_{-340}$ | $6.18^{+0.0505}_{-0.0489}$ | $44.0^{+0.0432}_{-0.045}$ | $0.05526^{+0.0262}_{-0.0374}$ | G395M |
| RUBIES_4233_47509 | 34.264602 | -5.232586 | 5.6718 | $2060^{+200}_{-180}$ | $6.83^{+0.0185}_{-0.0205}$ | $44.4^{+0.010}_{-0.010}$ | $0.2852^{+0.0053}_{-0.010}$ | G395M |
| RUBIES_4233_37124 | 214.990977 | 52.916524 | 5.6814 | $1450^{+280}_{-190}$ | $6.42^{+0.021}_{-0.0208}$ | $44.1^{+0.0353}_{-0.0396}$ | $0.3929^{+0.0256}_{-0.02}$ | G395M |
| RUBIES_4233_139709 | 34.296002 | -5.149895 | 5.6831 | $2770^{+310}_{-300}$ | $7.2^{+0.0173}_{-0.0197}$ | $44.5^{+0.0131}_{-0.0147}$ | $0.1459^{+0.0039}_{-0.00}$ | G395M |
| J0226_3325_3190 | 36.527690 | 3.041660 | 5.7345 | $1280^{+370}_{-250}$ | $6.19^{+0.0347}_{-0.0468}$ | $44.1^{+0.0211}_{-0.0308}$ | $0.5884^{+0.0293}_{-0.04}$ | G395M |
| JADES_1181_38147 | 189.270676 | 62.148418 | 5.8683 | $4550^{+10}_{-200}$ | $7.5^{+0.0195}_{-0.0187}$ | $44.2^{+0.010}_{-0.010}$ | $0.0398^{+0.0009}_{-0.00}$ | G395M |
| JADES_1181_61888 | 189.168016 | 62.217013 | 5.8752 | $1170^{+160}_{-100}$ | $6.03^{+0.0157}_{-0.0191}$ | $44.0^{+0.0117}_{-0.010}$ | $0.6799^{+0.0190}_{-0.010}$ | G395M |
| GDS_1210_13704 | 53.126535 | -27.818092 | 5.9189 | $2030^{+220}_{-160}$ | $6.56^{+0.0206}_{-0.0227}$ | $43.9^{+0.010}_{-0.010}$ | $0.1944^{+0.0044}_{-0.00}$ | G395M |
| JADES_1286_30148179 | 53.142082 | -27.779852 | 5.9214 | $1800^{+330}_{-330}$ | $6.34^{+0.0464}_{-0.049}$ | $44.1^{+0.0102}_{-0.010}$ | $0.4256^{+0.0353}_{-0.03}$ | G395M |
| MACS0416_4750_22011 | 64.079036 | -24.125954 | 5.9631 | $1470^{+100}_{-60}$ | $6.28^{+0.0107}_{-0.0141}$ | $43.9^{+0.010}_{-0.0114}$ | $0.3041^{+0.0070}_{-0.010}$ | G395M |
| GLIMPSE_9223_11026 | 342.197449 | -44.550621 | 5.9725 | $2440^{+170}_{-290}$ | $6.79^{+0.0203}_{-0.0137}$ | $44.1^{+0.010}_{-0.010}$ | $0.1450^{+0.0028}_{-0.00}$ | G395M |
| RUBIES_4233_174752 | 34.205808 | -5.100500 | 6.0389 | $1410^{+290}_{-240}$ | $6.35^{+0.0282}_{-0.0262}$ | $44.3^{+0.0122}_{-0.0124}$ | $0.6871^{+0.0265}_{-0.02}$ | G395M |
| GLIMPSE_9223_26653 | 342.184082 | -44.531643 | 6.1044 | $1110^{+80}_{-40}$ | $5.79^{+0.0108}_{-0.010}$ | $44.4^{+0.010}_{-0.010}$ | $3.2081^{+0.0864}_{-0.07}$ | G395M |
| RUBIES_4233_50716 | 34.313154 | -5.226781 | 6.1673 | $2840^{+800}_{-490}$ | $7.02^{+0.0506}_{-0.0574}$ | $44.1^{+0.0235}_{-0.0329}$ | $0.0875^{+0.0067}_{-0.010}$ | G395M |
| MACS1149_2758_30028 | 177.438019 | 22.470446 | 6.2117 | $2640^{+570}_{-640}$ | $6.71^{+0.0502}_{-0.0395}$ | $43.7^{+0.0307}_{-0.0206}$ | $0.0819^{+0.0059}_{-0.00}$ | G395M |
| GLIMPSE_9223_5536 | 342.256260 | -44.560186 | 6.2228 | $1950^{+390}_{-270}$ | $6.46^{+0.0206}_{-0.0381}$ | $43.8^{+0.014}_{-0.0243}$ | $0.1888^{+0.0052}_{-0.010}$ | G395M |
| RUBIES_4233_24210 | 215.066445 | 52.941877 | 6.2712 | $1250^{+590}_{-340}$ | $6.22^{+0.039}_{-0.049}$ | $44.3^{+0.0144}_{-0.0196}$ | $0.9811^{+0.0499}_{-0.05}$ | G395M |
| J0226_3325_10867 | 36.475139 | 3.081380 | 6.5341 | $2150^{+710}_{-480}$ | $6.73^{+0.0519}_{-0.0595}$ | $44.2^{+0.0226}_{-0.0254}$ | $0.2086^{+0.0122}_{-0.010}$ | G395M |
| J0226_3325_9556 | 36.495420 | 3.040207 | 6.5391 | $1960^{+470}_{-360}$ | $6.78^{+0.0375}_{-0.0366}$ | $44.3^{+0.0203}_{-0.0165}$ | $0.2515^{+0.0113}_{-0.010}$ | G395M |
| J0226_3325_6699 | 36.507805 | 3.049793 | 6.5405 | $3400^{+70}_{-40}$ | $8.3^{+0.010}_{-0.010}$ | $45.8^{+0.010}_{-0.010}$ | $0.2542^{+0.0011}_{-0.00}$ | G395M |
| J0910_2028_12910 | 137.727212 | -4.235207 | 6.6214 | $4280^{+40}_{-30}$ | $8.58^{+0.010}_{-0.010}$ | $45.9^{+0.010}_{-0.010}$ | $0.1742^{+0.0006}_{-0.00}$ | G395M |
| J0910_2028_14306 | 137.716790 | -4.214624 | 6.6334 | $1140^{+440}_{-180}$ | $6.03^{+0.0421}_{-0.0664}$ | $44.1^{+0.022}_{-0.0192}$ | $0.8870^{+0.0482}_{-0.05}$ | G395M |
| GLIMPSE_9223_329380 | 342.229976 | -44.510380 | 6.6388 | $1730^{+80}_{-80}$ | $6.78^{+0.010}_{-0.010}$ | $44.9^{+0.010}_{-0.010}$ | $1.1545^{+0.0114}_{-0.010}$ | G395M |
| RUBIES_4233_49140 | 214.892248 | 52.877410 | 6.6852 | $2910^{+50}_{-50}$ | $7.73^{+0.010}_{-0.010}$ | $45.1^{+0.010}_{-0.010}$ | $0.1917^{+0.0013}_{-0.00}$ | G395M |
| EGS_4106_57146 | 214.892246 | 52.877410 | 6.6859 | $3350^{+1890}_{-2180}$ | $7.63^{+0.010}_{-0.010}$ | $44.8^{+0.010}_{-0.010}$ | $0.1068^{+2.3411}_{-0.50}$ | G395M |
| EGS_4106_47962 | 214.892479 | 52.856891 | 6.7273 | $2430^{+200}_{-160}$ | $6.89^{+0.029}_{-0.0333}$ | $44.4^{+0.010}_{-0.0111}$ | $0.2360^{+0.0042}_{-0.00}$ | G395M |
| AURORA_1914_100182 | 189.177221 | 62.291510 | 6.7325 | $1660^{+470}_{-340}$ | $6.4^{+0.0415}_{-0.0622}$ | $44.4^{+0.010}_{-0.0101}$ | $0.8687^{+0.0706}_{-0.08}$ | G395M |
| JADES_1181_954 | 189.151966 | 62.259635 | 6.7608 | $2410^{+200}_{-150}$ | $7.11^{+0.0137}_{-0.0165}$ | $44.5^{+0.010}_{-0.010}$ | $0.2030^{+0.0036}_{-0.00}$ | G395M |
| RUBIES_4233_807469 | 34.376139 | -5.310366 | 6.7754 | $2330^{+890}_{-420}$ | $7.07^{+0.0228}_{-0.0306}$ | $44.5^{+0.0359}_{-0.0305}$ | $0.2151^{+0.0153}_{-0.010}$ | G395M |
| GLIMPSE_9223_46938 | 342.236053 | -44.541561 | 6.8526 | $1570^{+290}_{-210}$ | $6.13^{+0.0339}_{-0.0513}$ | $43.9^{+0.010}_{-0.010}$ | $0.5113^{+0.0253}_{-0.03}$ | G395M |
| RUBIES_4233_925921 | 215.075054 | 52.943828 | 6.9448 | $3220^{+640}_{-450}$ | $7.45^{+0.0281}_{-0.0306}$ | $44.6^{+0.0107}_{-0.0114}$ | $0.1144^{+0.0037}_{-0.00}$ | G395M |
| EGS_4287_127193 | 214.983029 | 52.955935 | 6.9833 | $3240^{+90}_{-90}$ | $7.73^{+0.010}_{-0.010}$ | $45.0^{+0.010}_{-0.010}$ | $0.1587^{+0.0013}_{-0.00}$ | G395M |
| RUBIES_4233_55604 | 214.983026 | 52.956001 | 6.9843 | $3320^{+80}_{-70}$ | $7.85^{+0.010}_{-0.010}$ | $45.2^{+0.010}_{-0.010}$ | $0.1751^{+0.0013}_{-0.00}$ | G395M |
| BLUEJAY_1810_19945 | 150.090563 | 2.381598 | 6.9894 | $2140^{+320}_{-270}$ | $6.95^{+0.0294}_{-0.0357}$ | $44.6^{+0.010}_{-0.0121}$ | $0.3739^{+0.0105}_{-0.010}$ | G395M |
| RUBIES_4233_42803 | 214.929524 | 52.887919 | 7.1522 | $3260^{+780}_{-760}$ | $7.36^{+0.0482}_{-0.0528}$ | $44.4^{+0.0188}_{-0.024}$ | $0.0923^{+0.0051}_{-0.010}$ | G395M |
| GDN_4762_33609 | 189.083488 | 62.202579 | 7.1883 | $2790^{+260}_{-240}$ | $7.39^{+0.0218}_{-0.0242}$ | $44.8^{+0.010}_{-0.010}$ | $0.1897^{+0.0028}_{-0.00}$ | G395M |

Notes: The list of identified BLAGNs ordered by redshift. The object ID is in the format of "Survey-name_Program-ID_Object-ID". Several objects have $\mathrm{FWHM_{H\alpha,broad}}$ slightly lower than 1000 km s$^{-1}$, but we still keep them since they were identified as BLAGNs in previous studies in the literature (e.g., Harikane et al. 2023; Maiolino et al. 2024). The last column indicates the main grating of the observations for detecting the strong emission lines. References for the initial JWST observation programs for these sources: AURORA (Shapley et al. 2025), BLUEJAY (Belli et al. 2024), CANUCS (Rihtaršič et al. 2025), CECILIA (Strom et al. 2023), CEERS (Finkelstein et al. 2025), EXCELS (Carnall et al. 2024), GLIMPSE (Kokorev et al. 2025), JADES (Eisenstein et al. 2023), LyC22 (Schaerer et al. 2021), RUBIES (de Graaff et al. 2025), and UNCOVER (Weaver et al. 2024).

*Facilities:* JWST(NIRSpec)

# APPENDIX

## A. ALL IDENTIFIED BLAGNS

Here we show the figures of all identified BLAGNs.

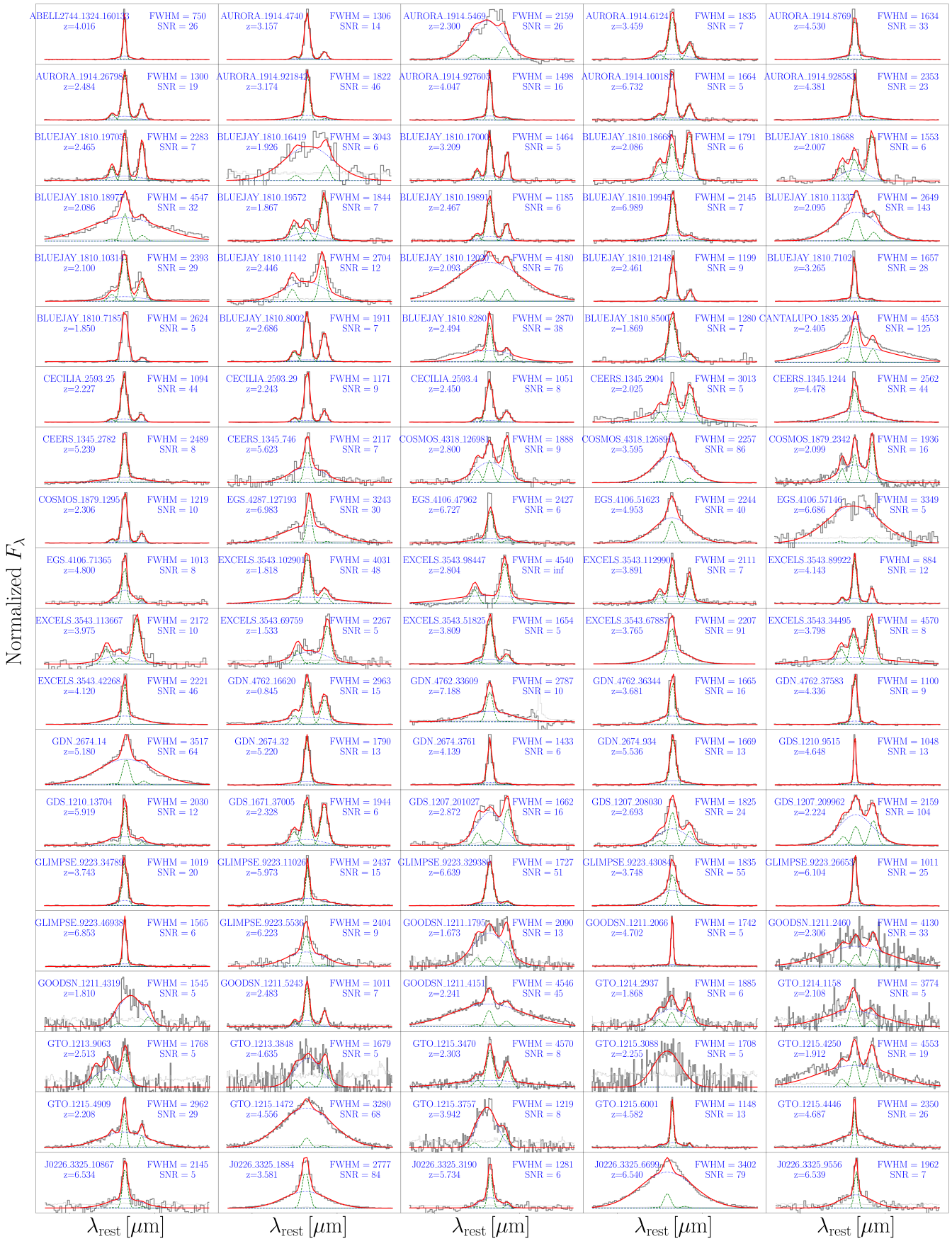


**Figure 7.** All identified BLAGNs. Data and error are shown in black and gray lines. Green-dashed and blue-dotted lines represent the narrow and broad components, respectively. The sum of both components are shown in red. For each galaxy, we also overlay their redshift, FWHM of the broad component (in $\mathrm{km\,s^{-1}}$), and line signal-to-noise.

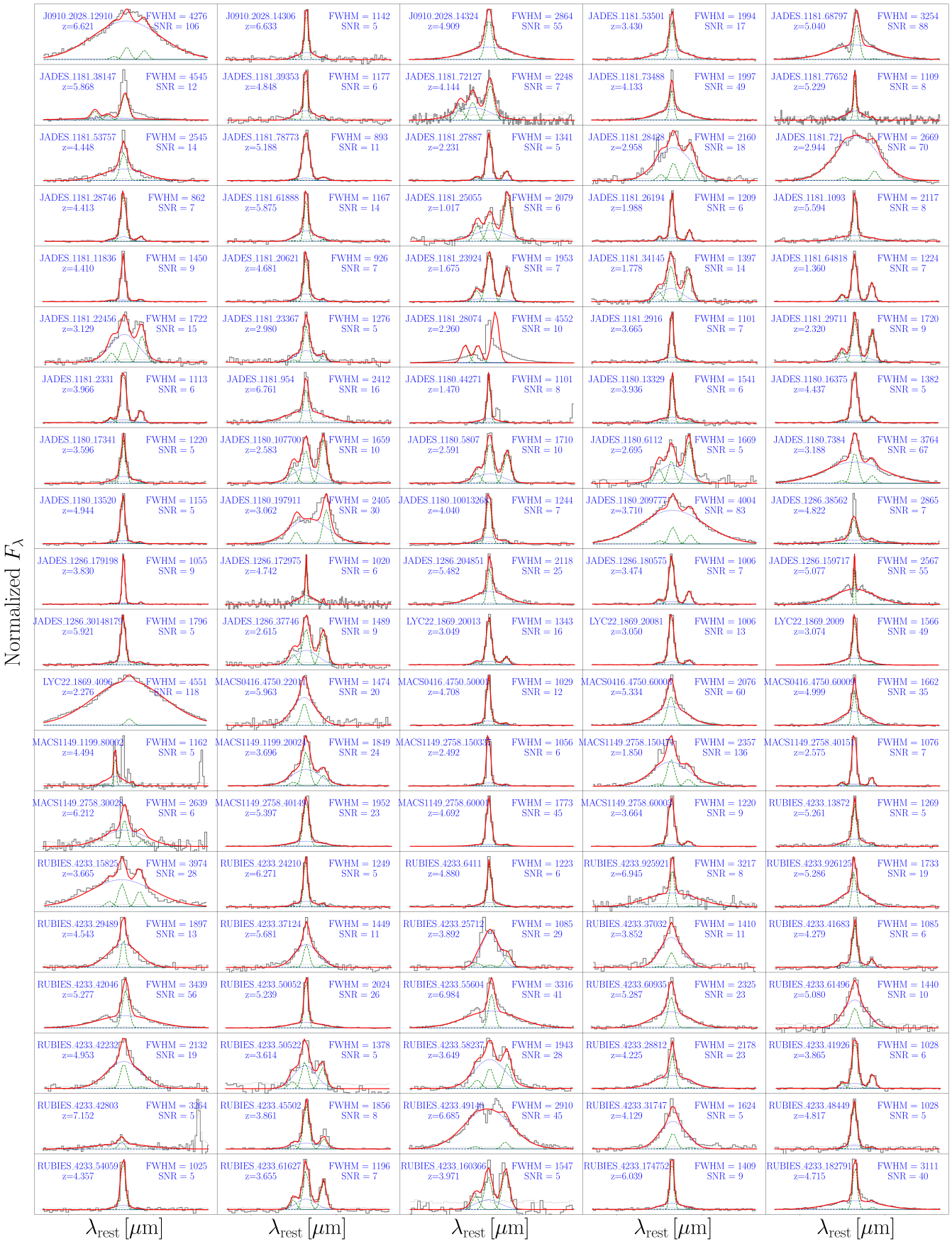


**Figure 8.** All identified BLAGNs cont.

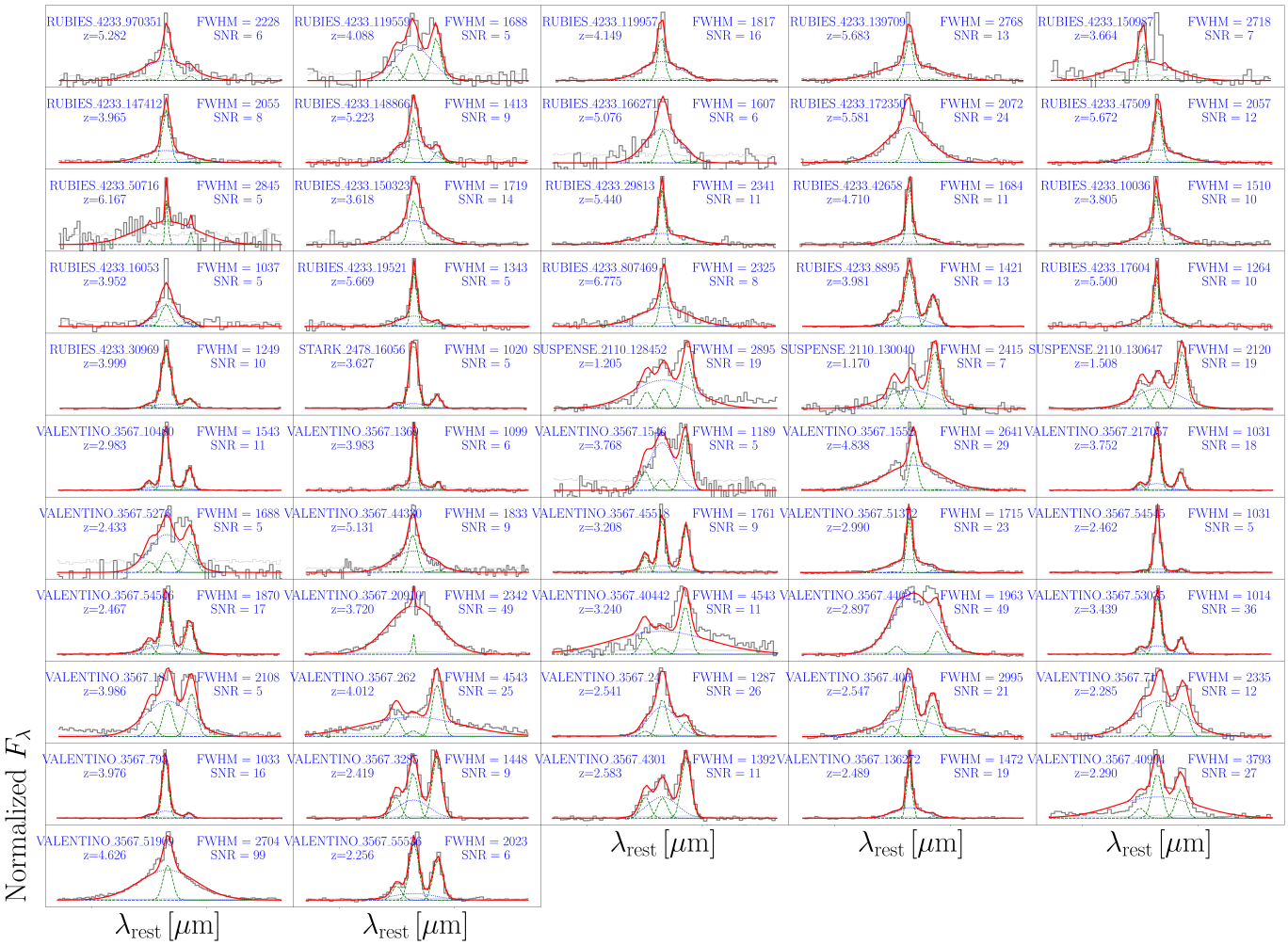


**Figure 9.** All identified BLAGNs cont.

## REFERENCES


Aggarwal, Y. 2024, MNRAS, 530, 1512, doi: 10.1093/mnras/stae914

Arevalo Gonzalez, F., Braun, T., Trussler, J., et al. 2025, arXiv e-prints, arXiv:2501.09585, doi: 10.48550/arXiv.2501.09585

Baldwin, J. A., Phillips, M. M., & Terlevich, R. 1981, PASP, 93, 5, doi: 10.1086/130766

Banados, E., Venemans, B. P., Mazzucchelli, C., et al. 2018, Nature, 553, 473, doi: 10.1038/nature25180

Beckwith, S. V. W., Stiavelli, M., Koekemoer, A. M., et al. 2006, AJ, 132, 1729, doi: 10.1086/507302

Belli, S., Park, M., Davies, R. L., et al. 2024, Nature, 630, 54, doi: 10.1038/s41586-024-07412-1

Brooks, M., Simons, R. C., Trump, J. R., et al. 2025, ApJ, 986, 177, doi: 10.3847/1538-4357/addac4

Bunker, A. J., et al. 2023, Monthly Notices of the Royal Astronomical Society, 518, 6011

Calzetti, D., Armus, L., Bohlin, R. C., et al. 2000, ApJ, 533, 682, doi: 10.1086/308692

Carnall, A. C., Cullen, F., McLure, R. J., et al. 2024, MNRAS, 534, 325, doi: 10.1093/mnras/stae2092

Chaussidon, E., Yèche, C., Palanque-Delabrouille, N., et al. 2023, ApJ, 944, 107, doi: 10.3847/1538-4357/acb3c2

Chien, T. C. C., Ling, C.-T., Goto, T., et al. 2024, MNRAS, 532, 719, doi: 10.1093/mnras/stae1550

Davies, R. I. 2007, MNRAS, 375, 1099, doi: 10.1111/j.1365-2966.2006.11383.x

de Graaff, A., Brammer, G., Weibel, A., et al. 2024, arXiv e-prints, arXiv:2409.05948, doi: 10.48550/arXiv.2409.05948

—. 2025, A&A, 697, A189, doi: 10.1051/0004-6361/202452186

Eisenstein, D. J., Willott, C., Alberts, S., et al. 2023, arXiv e-prints, arXiv:2306.02465, doi: 10.48550/arXiv.2306.02465

Ellis, R. S., McLure, R. J., Dunlop, J. S., et al. 2013, ApJL, 763, L7, doi: 10.1088/2041-8205/763/1/L7

Fabian, A. C. 2012, ARA&A, 50, 455, doi: 10.1146/annurev-astro-081811-125521

Finkelstein, S. L., Bagley, M. B., Arrabal Haro, P., et al. 2025, ApJL, 983, L4, doi: 10.3847/2041-8213/adbbd3

Goulding, A. D., Greene, J. E., Setton, D. J., et al. 2023, ApJL, 955, L24, doi: 10.3847/2041-8213/acf7c5

Greene, J. E., & Ho, L. C. 2005, ApJ, 630, 122, doi: 10.1086/431897

Greene, J. E., Labbe, I., Goulding, A. D., et al. 2024, ApJ, 964, 39, doi: 10.3847/1538-4357/ad1e5f

Greene, J. E., Setton, D. J., Furtak, L. J., et al. 2025, arXiv e-prints, arXiv:2509.05434, doi: 10.48550/arXiv.2509.05434

Grogin, N. A., Kocevski, D. D., Faber, S. M., et al. 2011, ApJS, 197, 35, doi: 10.1088/0067-0049/197/2/35

Hardcastle, M. J., & Croston, J. H. 2020, NewAR, 88, 101539, doi: 10.1016/j.newar.2020.101539

Harikane, Y., Zhang, Y., Nakajima, K., et al. 2023, ApJ, 959, 39, doi: 10.3847/1538-4357/ad029e

He, W., Akiyama, M., Enoki, M., et al. 2024, ApJ, 962, 152, doi: 10.3847/1538-4357/ad1518

Heintz, K. E., Watson, D., Brammer, G., et al. 2024, Science, 384, 890, doi: 10.1126/science.adj0343

Hopkins, P. F., Hernquist, L., Cox, T. J., et al. 2006, ApJS, 163, 1, doi: 10.1086/499298

Juodžbalis, I., Maiolino, R., Baker, W. M., et al. 2025, arXiv e-prints, arXiv:2504.03551, doi: 10.48550/arXiv.2504.03551

Kauffmann, G., Heckman, T. M., Tremonti, C., et al. 2003, MNRAS, 346, 1055, doi: 10.1111/j.1365-2966.2003.07154.x

Kewley, L. J., Dopita, M. A., Sutherland, R. S., Heisler, C. A., & Trevena, J. 2001, ApJ, 556, 121, doi: 10.1086/321545

Kocevski, D. D., Onoue, M., Inayoshi, K., et al. 2023, ApJL, 954, L4, doi: 10.3847/2041-8213/ace5a0

Kocevski, D. D. e. a. 2022, arXiv e-prints

Koekemoer, A. M., Donley, J., Grogin, N., et al. 2011, in American Astronomical Society Meeting Abstracts, Vol. 218, American Astronomical Society Meeting Abstracts #218, 328.03

Kokorev, V., Atek, H., Chisholm, J., et al. 2025, ApJL, 983, L22, doi: 10.3847/2041-8213/adc458

Kormendy, J., & Ho, L. C. 2013, ARA&A, 51, 511, doi: 10.1146/annurev-astro-082708-101811

Laha, S., Reynolds, C. S., Reeves, J., et al. 2021, Nature Astronomy, 5, 13, doi: 10.1038/s41550-020-01255-2

Lambrides, E., Garofali, K., Larson, R., et al. 2024, arXiv e-prints, arXiv:2409.13047, doi: 10.48550/arXiv.2409.13047

Lin, X., Wang, F., Fan, X., et al. 2024, ApJ, 974, 147, doi: 10.3847/1538-4357/ad6565

Lu, K.-X., Li, Y.-R., Wu, Q., et al. 2025, ApJS, 276, 51, doi: 10.3847/1538-4365/ad9a5a

Maiolino, R., Scholtz, J., Curtis-Lake, E., et al. 2024, A&A, 691, A145, doi: 10.1051/0004-6361/202347640

Matsuoka, Y., Onoue, M., Kashikawa, N., et al. 2019, ApJL, 872, L2, doi: 10.3847/2041-8213/ab0216

Matthee, J., Naidu, R. P., Brammer, G., et al. 2023

McConnell, N. J., & Ma, C.-P. 2013, ApJ, 764, 184, doi: 10.1088/0004-637X/764/2/184

McLure, R. J., & Dunlop, J. S. 2004, MNRAS, 352, 1390, doi: 10.1111/j.1365-2966.2004.08034.x

Mortlock, D. J., Warren, S. J., Venemans, B. P., et al. 2011, Nature, 474, 616, doi: 10.1038/nature10159

Mountrichas, G. 2023, A&A, 672, A98, doi: 10.1051/0004-6361/202345924

Nakajima, K., Ouchi, M., Isobe, Y., et al. 2023, ApJS, 269, 33, doi: 10.3847/1538-4365/acd556

Napolitano, L., Castellano, M., Pentericci, L., et al. 2025, A&A, 693, A50, doi: 10.1051/0004-6361/202452090

Oesch, P. A., Brammer, G., van Dokkum, P. G., et al. 2016, The Astrophysical Journal, 819, 129

Onoue, M., Kashikawa, N., Matsuoka, Y., et al. 2019, ApJ, 880, 77, doi: 10.3847/1538-4357/ab29e9

Osterbrock, D. E., & Ferland, G. J. 2006, Astrophysics of gaseous nebulae and active galactic nuclei

Pâris, I., Petitjean, P., Aubourg, É., et al. 2018, A&A, 613, A51, doi: 10.1051/0004-6361/201732445

Planck Collaboration, Aghanim, N., Akrami, Y., et al. 2020, A&A, 641, A6, doi: 10.1051/0004-6361/201833910

Rihtaršič, G., Bradač, M., Desprez, G., et al. 2025, A&A, 696, A15, doi: 10.1051/0004-6361/202451117

Risaliti, G., & Elvis, M. 2004, in Astrophysics and Space Science Library, Vol. 308, Supermassive Black Holes in the Distant Universe, ed. A. J. Barger, 187, doi: 10.1007/978-1-4020-2471-9_6

Rousselot, P., Lidman, C., Cuby, J. G., Moreels, G., & Monnet, G. 2000, A&A, 354, 1134

Schaerer, D., Atek, H., Chisholm, J., et al. 2021, LyC22 - Deep spectroscopic insights on star-forming galaxies 2.2 Gyr after the Big Bang, JWST Proposal. Cycle 1, ID. #1869

Shapley, A. E., Sanders, R. L., Topping, M. W., et al. 2025, ApJ, 980, 242, doi: 10.3847/1538-4357/adad68

Shen, Y., Wu, J., Jiang, L., et al. 2019, ApJ, 873, 35, doi: 10.3847/1538-4357/ab03d9

Silk, J., & Rees, M. J. 1998, A&A, 331, L1, doi: 10.48550/arXiv.astro-ph/9801013

Storey, P. J., & Zeippen, C. J. 2000, MNRAS, 312, 813, doi: 10.1046/j.1365-8711.2000.03184.x

Strom, A. L., Rudie, G. C., Trainor, R. F., et al. 2023, ApJL, 958, L11, doi: 10.3847/2041-8213/ad07dc

Suh, H., Scharwächter, J., Farina, E. P., et al. 2025, Nature Astronomy, 9, 271, doi: 10.1038/s41550-024-02402-9

Taylor, A. J., Finkelstein, S. L., Kocevski, D. D., et al. 2024, arXiv e-prints, arXiv:2409.06772

Trakhtenbrot, B., Netzer, H., Lira, P., & Shemmer, O. 2011, ApJ, 730, 7, doi: 10.1088/0004-637X/730/1/7

Übler, H., Maiolino, R., Curtis-Lake, E., et al. 2023, A&A, 677, A145, doi: 10.1051/0004-6361/202346137

Valentino, F., Heintz, K. E., Brammer, G., et al. 2025, A&A, 699, A358, doi: 10.1051/0004-6361/202553908

Weaver, J. R., Cutler, S. E., Pan, R., et al. 2024, ApJS, 270, 7, doi: 10.3847/1538-4365/ad07e0

Willott, C. J., Albert, L., Arzoumanian, D., et al. 2010, The Astronomical Journal, 140, 546

Windhorst, R. A., Cohen, S. H., Hathi, N. P., et al. 2011, ApJS, 193, 27, doi: 10.1088/0067-0049/193/2/27

Wu, Q., & Shen, Y. 2022, ApJS, 263, 42, doi: 10.3847/1538-4365/ac9ead